# Chapter 4

# TRIGA REACTOR

The reactor design bases are predicted on the maximum operational capability for the fuel elements and configuration described in this report. The TRIGA reactor system has three major areas which are used to define the reactor design bases:

a. Fuel temperature,

b. Prompt negative temperature coefficient,

c. Reactor power.

Of these three only one, fuel temperature, is a real limitation. A summary is presented below of the conclusions obtained from the reactor design bases described in this section.

## 4.1. DESIGN BASES

The fuel temperature is a limit in both steady-state and pulse mode operation. This limit stems from the out-gassing of hydrogen from U-ZrH (H/Zr ; x) fuel and the subsequent stress produced in the fuel element clad material. The strength of the clad as a function of temperature can set the upper limit on the fuel temperature. Fuel temperature limits of 1150°C (with clad $\leq$ 500°C) and 970°C (with clad $\geq$ 500°C) for U-ZrH (H/Zr ; 1.65) have been set to preclude the loss of clad integrity. Simnad [34] summarizes the properties of U-$ZrH_x$ fuel materials for TRIGA reactors, including the limiting design bases and parameters.

The basic parameter which provides the TRIGA system with a large safety factor in steady-state operation and under transient conditions is the prompt negative temperature coefficient which is rather constant with temperature (~0.01% $\delta k/k°C$), as described later. This coefficient is a function of the fuel composition and core geometry.

Fuel and clad temperature limit the operation of the reactor. However, it is more convenient to set a power level limit which is based on temperature. The design bases analysis indicates that operation at up to 1900 kW (with an 85 element core and 120°F inlet water temperature) with natural convective flow will not allow film boiling, and therefore high fuel and clad temperatures which could cause loss of clad integrity could not occur.

### 4.1.1 Reactor Fuel Temperature

The basic safety limit for the TRIGA reactor system is the fuel temperature; this applies for both the steady-state and pulse mode of operation.

Two limiting temperatures are of interest, depending on the type of TRIGA fuel used. The TRIGA fuel which is considered low hydride, that with an H/Zr ratio of less than 1.5, has a lower temperature limit than fuel with a higher H/Zr ratio. Figure 4-1 indicates that the higher hydride compositions are single phase and are not subject to the large volume changes associated with the phase transformations at approximately 530°C in the lower hydrides. Also, it has been noted [1] that the higher hydrides lack any significant thermal diffusion of hydrogen. These two facts preclude concomitant volume changes. The important properties of delta phase U-ZrH are given in Table 4-1.

Table 4-1

PHYSICAL PROPERTIES OF DELTA PHASE U-ZrH

| | |
|---|---|
| Thermal conductivity (93°C - 650°C) | 13 Btu/hr-ft$^2$-°F |
| Elastic modulus: 20°C | 9.1 x $10^6$ psi |
| 650°C | 6.0 x $10^6$ psi |
| Ultimate tensile strength (to 650°C) | 24,000 psi |
| Compressive strength (20°C) | 60,000 psi |
| Compressive yield (20°C) | 35,000 psi |
| Heat of formation ($\delta H^o_f$ 298°C) | 37.72 kcal/g-mole |

Among the chemical properties of U-ZrH and ZrH, the reaction rate of the hydride with water is of particular interest. Since the hydriding reaction is exothermic, water will react more readily with zirconium than with zirconium hydride systems. Zirconium is frequently used in contact with water in reactors, and the zirconium-water reaction is not a safety hazard. Experiments carried out at GA Technologies show that the zirconium hydride systems have a relatively low chemical reactivity with respect to water and air. These tests have involved the quenching with water of both powders and solid specimens of U-ZrH after heating to as high as 850°C, and of solid U-Zr alloy after heating to as high as 1200°C. Tests have also been made to determine the extent to which fission products are removed from the surfaces of the fuel elements at room temperature. Results prove that, because of the high resistance to leaching, a large fraction of the fission products is retained in even completely unclad U-ZrH fuel.

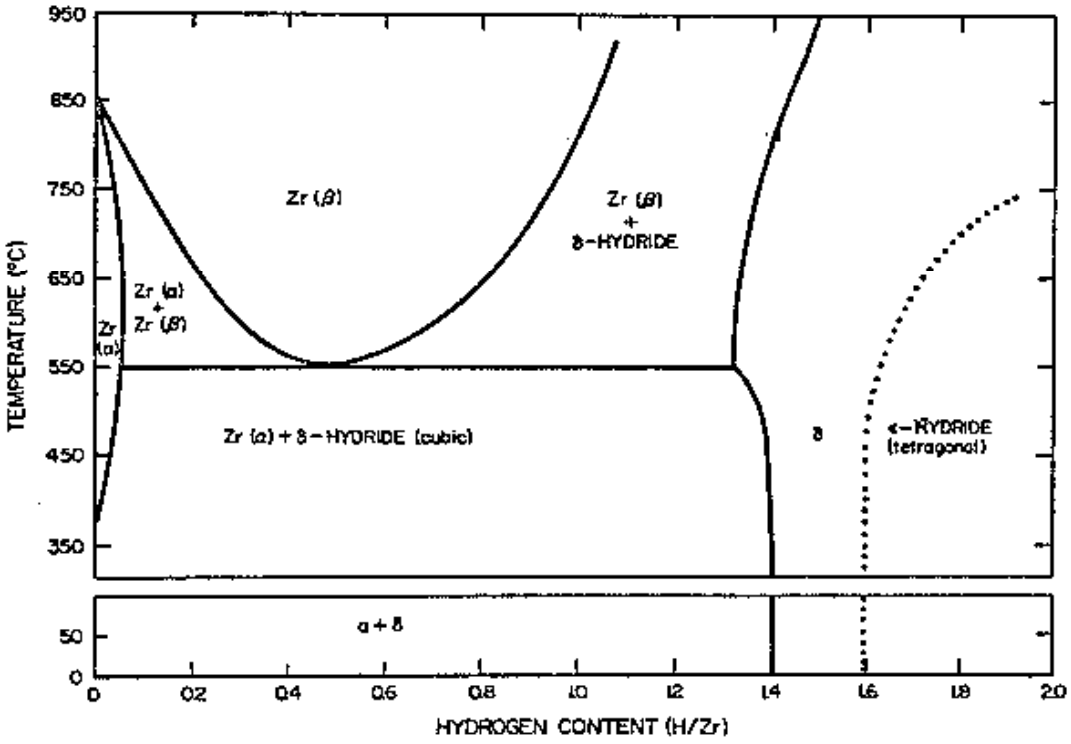


PHASE DIAGRAM OF THE
ZIRCONIUM-HYDROGEN SYSTEM

Figure 4-1

For the rest of the discussion of fuel temperatures, we will concern ourselves with the higher hydride (H/Zr $\geq$ 1.5) TRIGA fuel clad with 304 stainless steel 0.020 in. (0.508 mm) thick, or a cladding material equivalent in strength at the temperatures discussed.

At room temperature the hydride is like ceramic and shows little ductility. However, at the elevated temperatures of interest for pulsing, the material is found to be more ductile. The effect of very large thermal stress on hydride fuel bodies has been observed in hot cell observations to cause relatively widely spaced cracks which tend to be either radial or normal to the central axis and do not interfere with radial heat flow. Since the segments tend to be orthogonal, their relative positions appear to be quite stable.

The limiting effect of fuel temperature then is the hydrogen gas over pressure. Figure 4-2 relates equilibrium hydrogen pressure over the fuel as a function of temperature for material with three different H/Zr ratios.

The hydrogen gas over pressure is not in itself detrimental but if the stress produced by the gas pressure within the fuel can exceeds the ultimate strength of the clad material, a rupture of the fuel clad could occur. While the final conditions of fuel temperature and hydrogen pressure in which such an occurrence could come about are of interest, the mechanisms in obtaining temperatures and pressures of concern are different in the pulsing and steady-state mode of operation, and each mechanism will be discussed independently of the other.

In this discussion it will be assumed that the fuel consists of U-ZrH (H/Zr ; 1.65) with the uranium being 8.5 wt. % and further that the cladding can is 304 stainless steel. The clad thickness is 0.020 in. (0.508 mm) with an inside clad diameter of 1.43 in. (3.63 cm). These fuel parameters have been chosen since they represent the nominal specifications for TRIGA fuel elements. Figure 4-3 shows the characteristic of 304 stainless steel with regard to yield and ultimate strengths as a function of temperature.

In determining the stress applied to the cladding from the internal hydrogen gas pressure the equation

$$S = P\, r/t\ , \qquad (1)$$

applies where

S = stress in psi,

P = internal pressure in psi,

r = radius of the cladding can,

t = wall thickness of the clad.

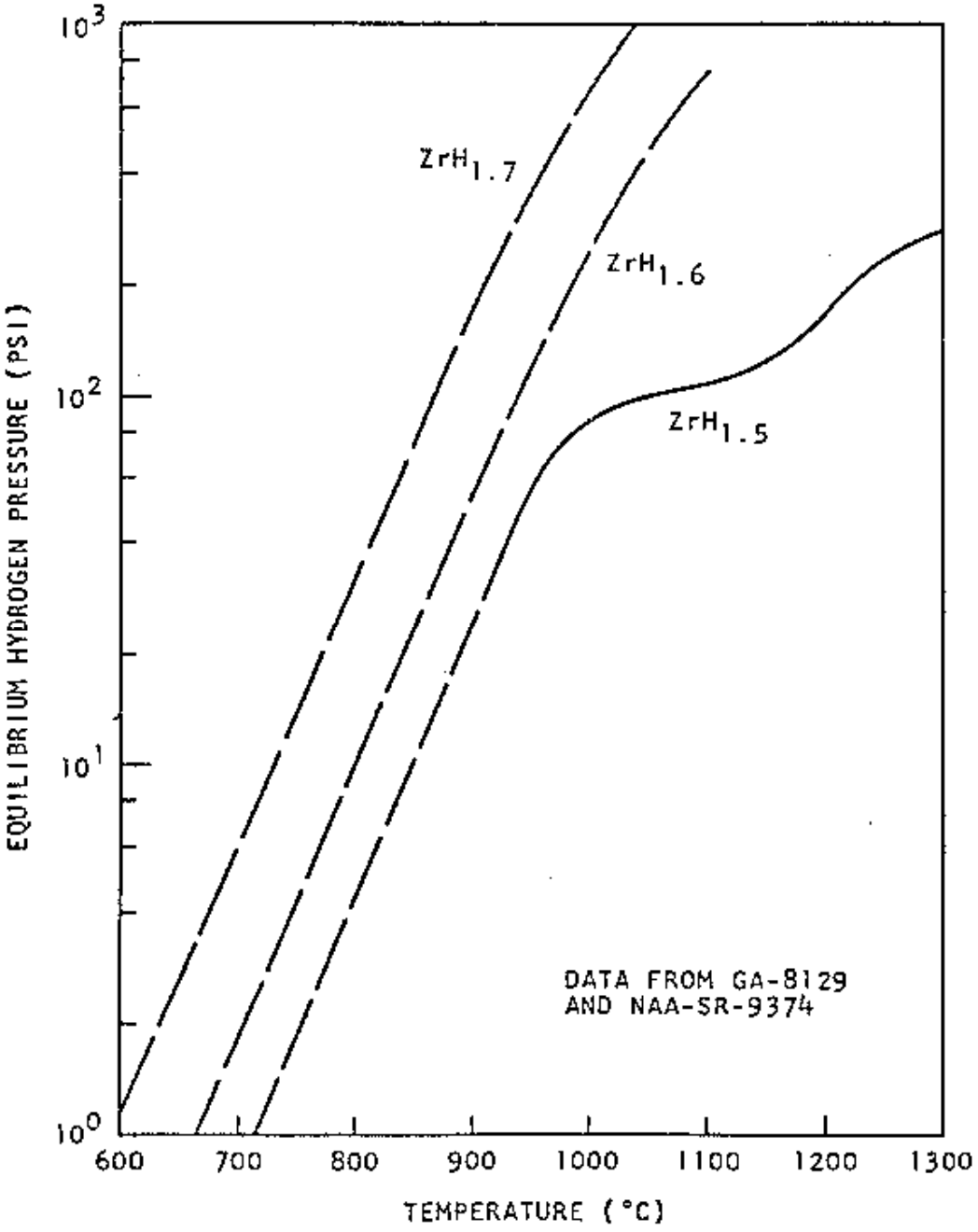


EQUILIBRIUM HYDROGEN PRESSURE
VERSUS TEMPERATURE FOR ZIRCONIUM-HYDROGEN

Figure 4-2

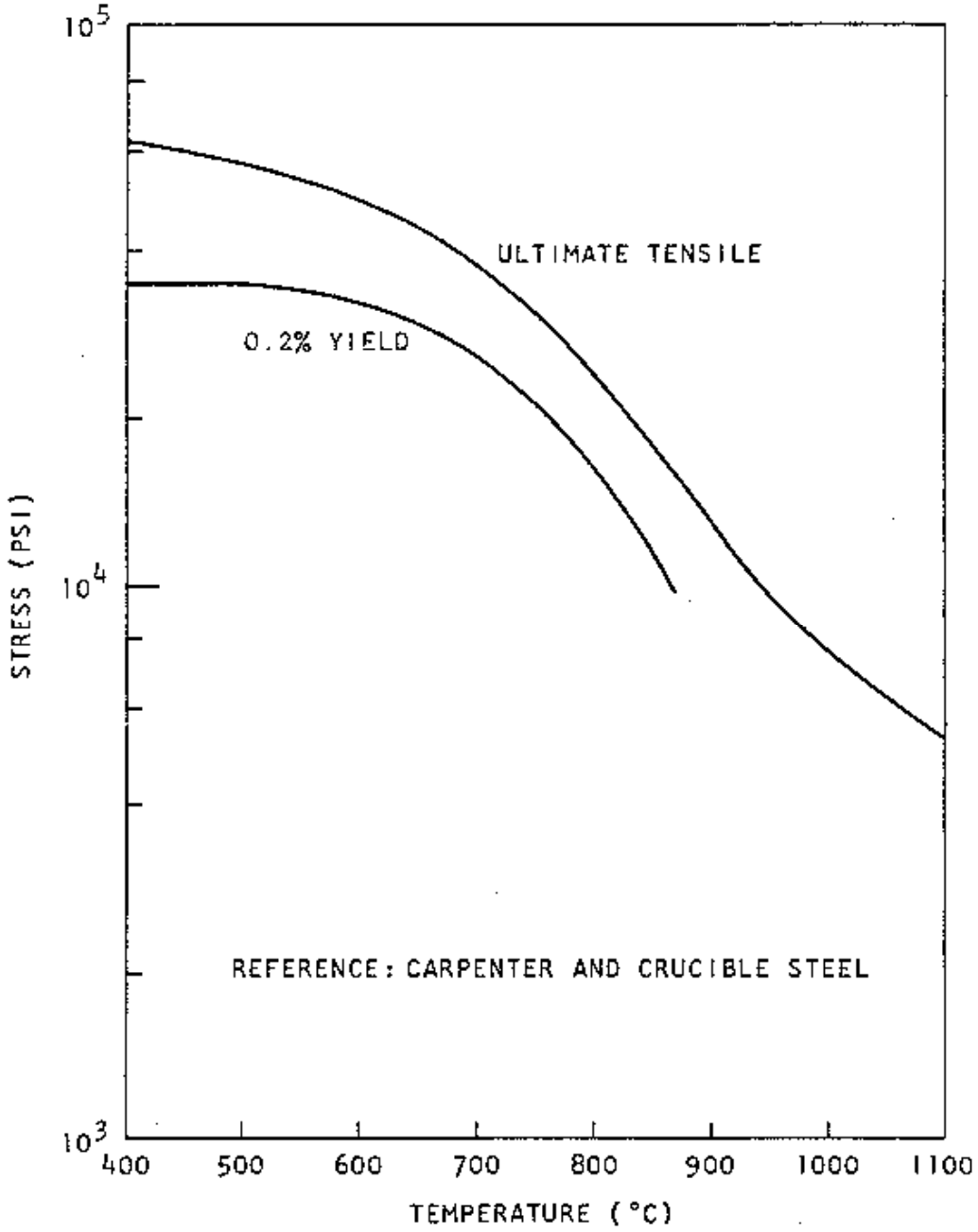


STRENGTH OF TYPE 304 STAINLESS STEEL
AS A FUNCTION OF TEMPERATURE

Figure 4-3

Then for the cladding we have approximately

$$S = 36.7\ P\ , \qquad (2)$$

or the stress applied to the clad is approximately 36.7 times the internal pressure.

It is of interest to relate the strength of the clad material at its operating temperature to the stress applied to the clad from the internal gas pressure associated with the fuel temperature. Figure 4-4 gives information as to the ultimate clad strength as a function of temperature and also describes the stress applied to the clad as a result of hydrogen dissociation for fuel having a H/Zr ratio of 1.65 as a function of temperature.

There are several reasons why the gas pressure should be less for the transient conditions than the equilibrium condition values would predict. For example, the gas diffusion rates are finite; surface cooling is believed to be caused by endothermic gas emission which tends to lower the diffusion constant at the surface; reabsorption takes place concurrently on the cooler hydride surfaces away from the hot spot; there is evidence for a low permeability oxide film on the fuel surface; and some local heat transfer does take place during the pulse time to cause a less than adiabatic true surface temperature.

4.1.1.1 Fuel and Clad Temperature. The following discussion relates the element clad temperature and the maximum fuel temperature during a short time after a pulse.

The radial temperature distribution in the fuel element immediately following a pulse is very similar to the power distribution shown in Figure 4-5. This initial steep thermal gradient at the fuel surface results in some heat transfer during the time of the pulse so that the true peak temperature does not quite reach the adiabatic peak temperature. A large temperature gradient is also impressed upon the clad which can result in a high heat flux from the clad into the water. If the heat flux is sufficiently high, film boiling may occur and form an insulating jacket of steam around the fuel elements permitting the clad temperature to tend to approach the fuel temperature. Evidence has been obtained experimentally which shows that film boiling has occurred occasionally for some fuel elements in the Advanced TRIGA Prototype Reactor located at GA Technologies [2]. The consequence of this film boiling was discoloration of the clad surface.

Thermal transient calculations were made using the RAT computer code. RAT is a 2-D transient heat transport code developed to account for fluid flow and temperature dependent material properties. Calculations show that if film boiling occurs after a pulse it may take place either at the time of maximum heat flux from the clad, before the bulk temperature of the coolant has changed appreciably, or it may take place at a much later time when the bulk temperature of the coolant has approached the saturation temperature, resulting in a markedly reduced threshold for film boiling. Data obtained by Johnson et al. [3] for

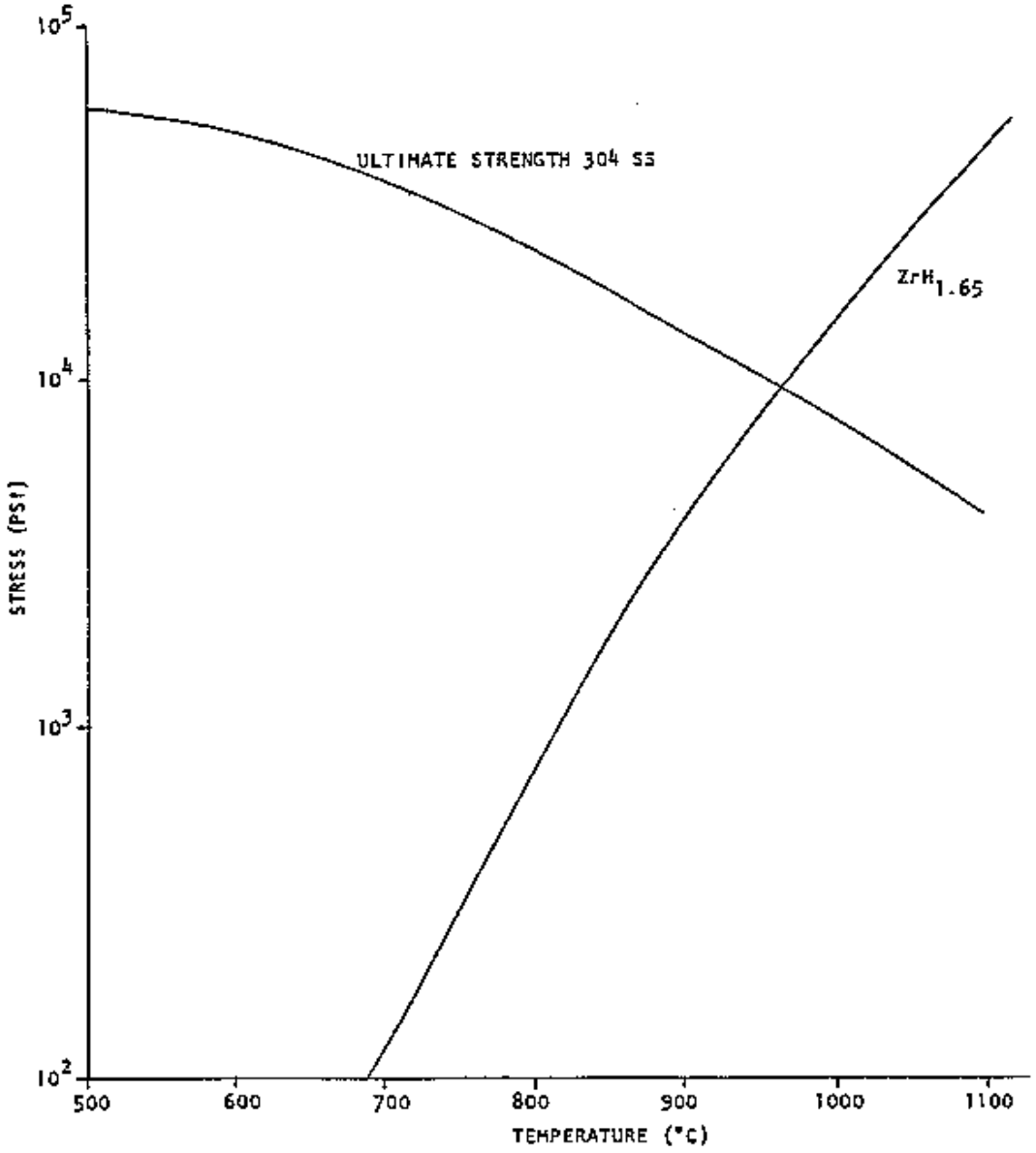


STRENGTH AND APPLIED STRESS AS A FUNCTION OF
TEMPERATURE, EQUILIBRIUM HYDROGEN DISSOCIATION PRESSURE

Figure 4-4

transient heating of ribbons in 100°F water, showed burnout fluxes of 0.9 to 2.0 MBtu/ft$^2$-hr for e-folding periods from 5 to 90 milliseconds. On the other hand, sufficient bulk heating of the coolant channeled between fuel elements can take place in several tenths of a second to lower the departure from nucleate boiling (DNB) point to approximately 0.4 MBtu/ft$^2$-hr. It is shown, on the basis of the following analysis, that the second mode is the most likely; i.e., when film boiling occurs it takes place under essentially steady-state conditions at local water temperatures near saturation.

A value for the temperature that may be reached by the clad if film boiling occurs was obtained in the following manner. A transient thermal calculation was performed using the radial and axial power distributions in Figure 4-5 and Figure 4-6, respectively, under the assumption that the thermal resistance at the fuel-clad interface was nonexistent. A boiling heat transfer model, as shown in Figure 4-7, was used in order to obtain an upper limit for the clad temperature rise. The model used the data of McAdams [4] for the subcooled boiling and the work of Sparrow and Cess [5] for the film boiling regime. A conservative estimate was obtained for the minimum heat flux in film boiling by using the correlations of Speigler et al. [6], Zuber [7], and Rohsenow and Choi [8] to find the minimum temperature point at which film boiling could occur. This calculation gave an upper limit of 760°C clad temperature for a peak initial fuel temperature of 1000°C, as shown in Figure 4-8. Fuel temperature distributions for this case are shown in Figure 4-9 and the heat flux into the water from the clad is shown in Figure 4-10. In this limiting case, DNB occurred only 13 milliseconds after the pulse, conservatively calculated assuming a steady-state DNB correlation. Subsequently, experimental transition and film boiling data were found to have been reported by Ellion [9] for water conditions similar to those for the TRIGA system. The Ellion data show the minimum heat flux, used in the limiting calculation described above, was conservative by a factor of 5. An appropriate correction was made which resulted in a more realistic estimate of 470°C as the maximum clad temperature expected if film boiling occurs. This result is in agreement with experimental evidence obtained for clad temperatures of 400°C to 500°C for TRIGA Mark F fuel elements which have been operated under film boiling conditions [10].

The preceding analysis assessing the maximum clad temperatures associated with film boiling assumed no thermal resistance at fuel-clad interface. Measurements of fuel temperatures as a function of steady-state power level provide evidence that after operating at high fuel temperatures, a permanent gap is produced between the fuel body and the clad by fuel expansion. This gap exists at all temperatures below the maximum operating temperature. (See, for example, Figure 16 in Reference 10.) The gap thickness varies with fuel temperature and clad temperature so that cooling of the fuel or overheating of the clad tends to widen the gap and decrease the heat transfer rate. Additional thermal resistance due to oxide and other films on the fuel and clad surfaces is expected. Experimental and theoretical studies of thermal contact resistance have been reported [11-13] which provide insight into the mechanisms involved. They do not, however, permit quantitative prediction of this application because the basic data required for input

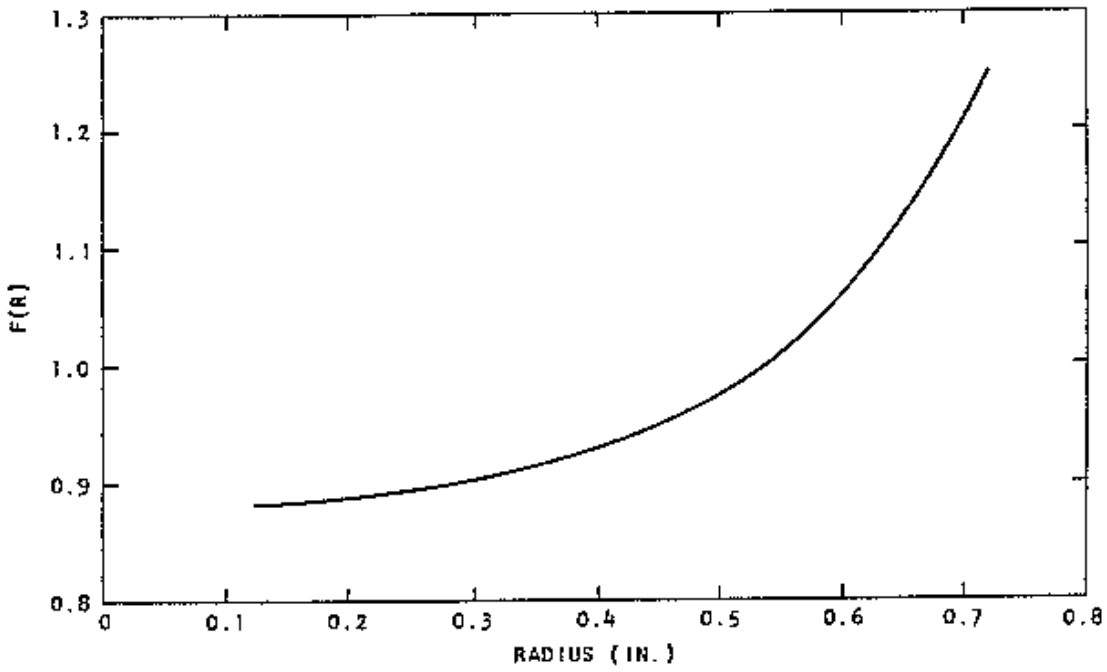


RADIAL POWER DISTRIBUTION IN
THE U-ZrH FUEL ELEMENT

Figure 4-5

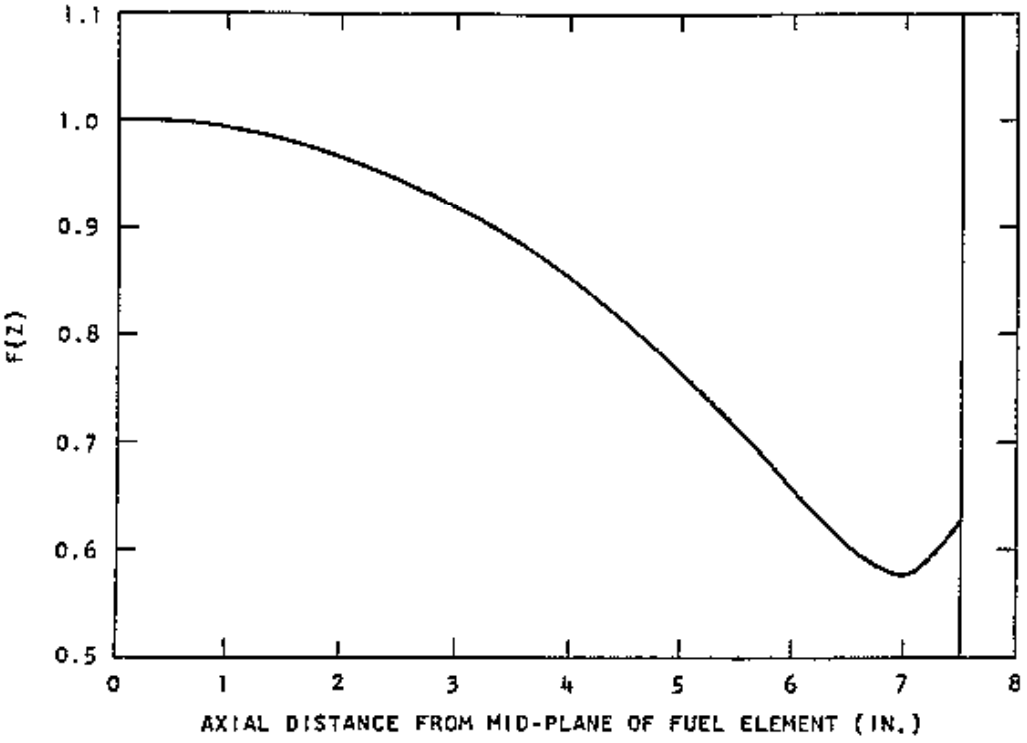


AXIAL POWER DISTRIBUTION IN
THE U-ZrH FUEL ELEMENT

Figure 4-6

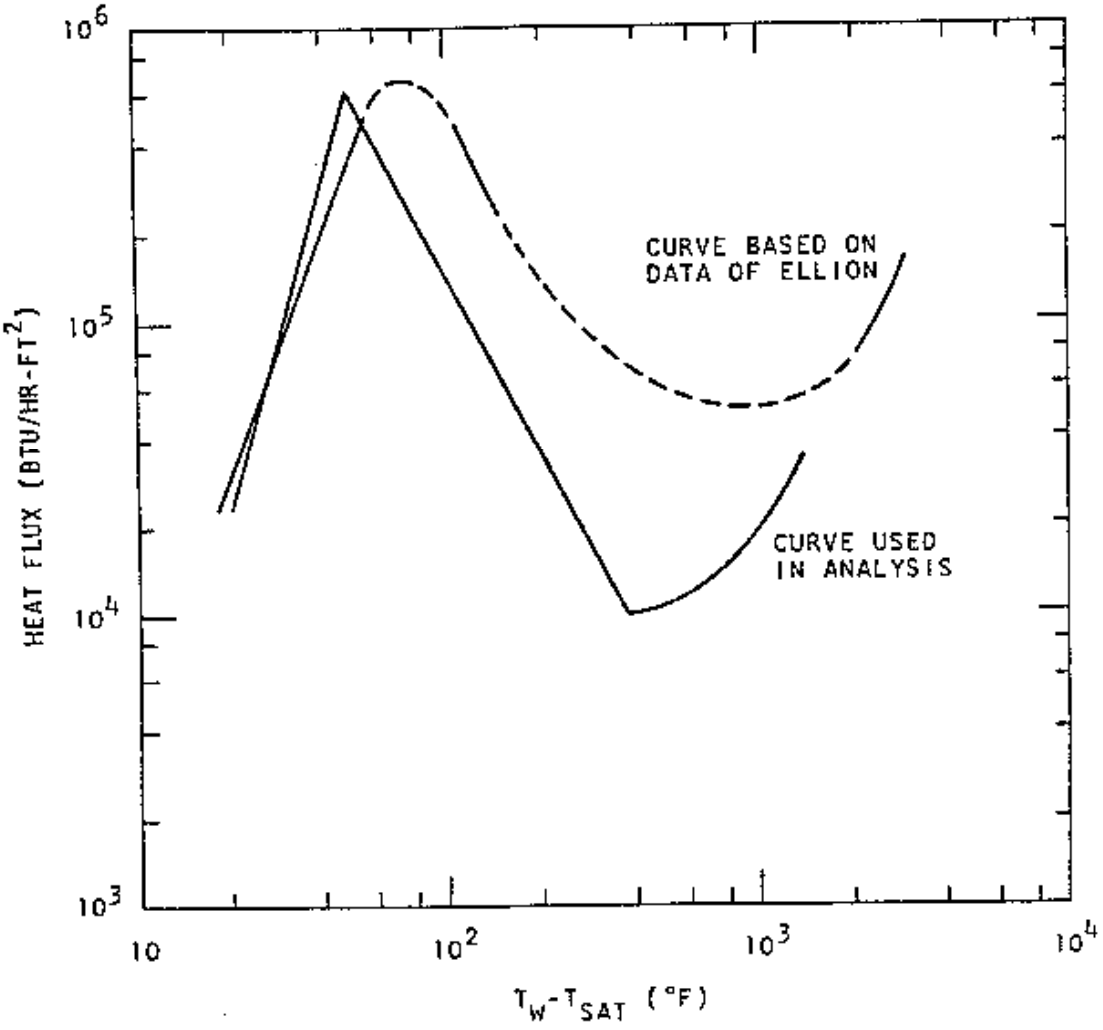


SUBCOOLED BOILING HEAT TRANSFER FOR WATER

Figure 4-7

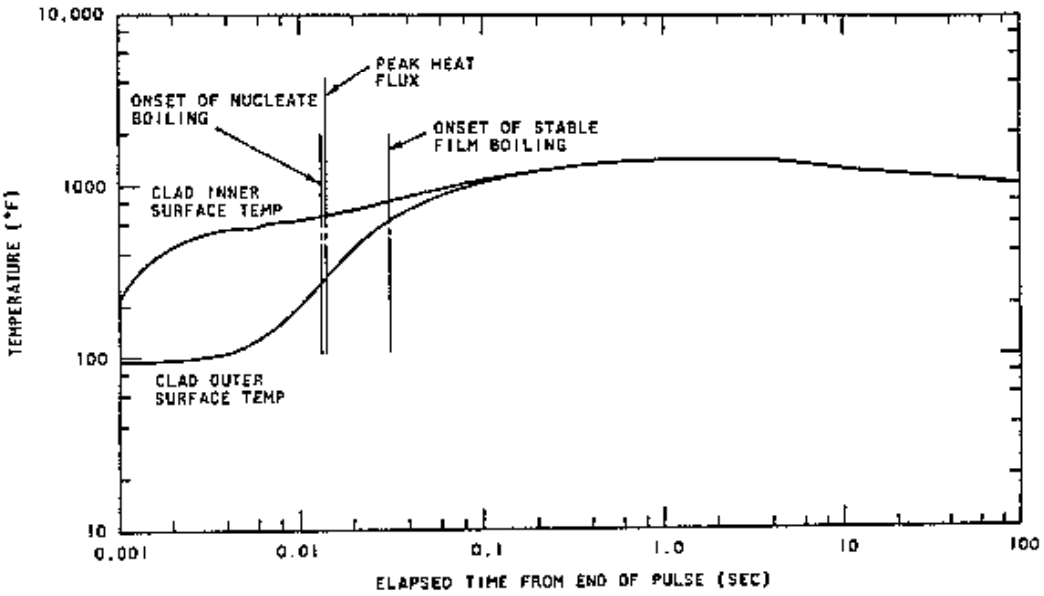


CLAD TEMPERATURE AT MIDPOINT OF
WELL-BONDED FUEL ELEMENT

Figure 4-8

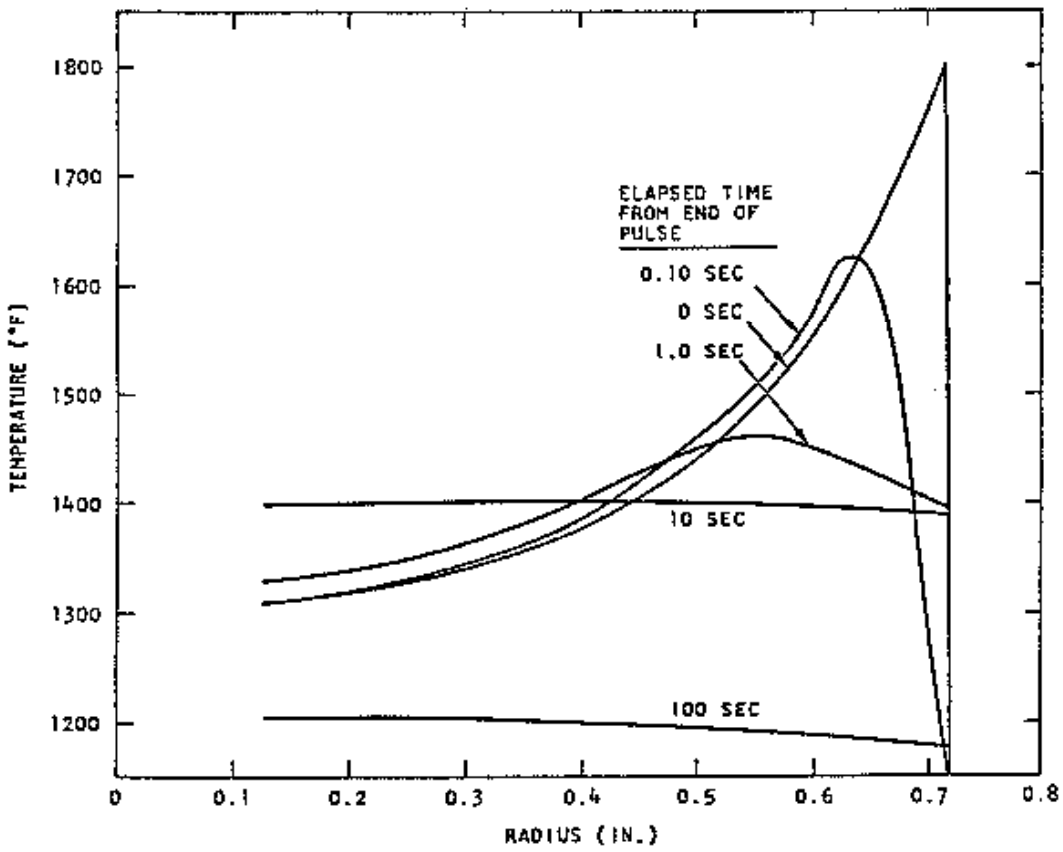


FUEL BODY TEMPERATURES AT MIDPLANE OF WELL-BONDED FUEL ELEMENT AFTER A PULSE

Figure 4-9

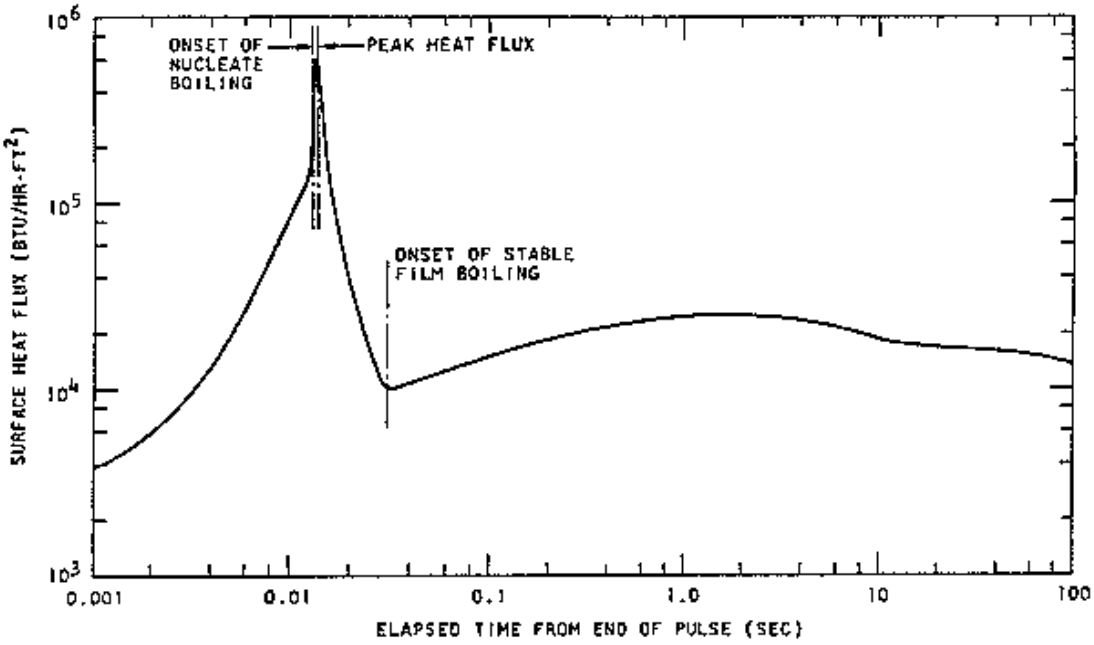


SURFACE HEAT FLUX AT MIDPLANE OF WELL-BONDED
FUEL ELEMENT AFTER A PULSE

Figure 4-10

are presently not fully known. Instead, several transient thermal computations were made using the RAT code. Each of these was made with an assumed value for the effective gap conductance, in order to determine the effective gap coefficient for which departure from nucleate boiling is incipient. These results were then compared with the incipient film boiling conditions of the 1000°C peak fuel temperature case.

For convenience, the calculations were made using the same initial temperature distribution as was used for the preceding calculation. The calculations assumed a coolant flow velocity of 1 ft per second, which is within the range of flow velocities computed for natural convection under various steady-state conditions for these reactors. The calculations did not use a complete boiling curve heat transfer model, but instead, included a convection cooled region (no boiling) and a subcooled nucleate boiling region without employing an upper DNB limit. The results were analyzed by inspection using the extended steady-state correlation of Bernath [14] which has been reported by Spano [15] to give agreement with SPERT II burnout results within the experimental uncertainties in flow rate.

The transient thermal calculations were performed using effective gap conductances of 500, 375, and 250 Btu/hr-ft$^2$-°F. The resulting wall temperature distributions were inspected to determine the axial wall position and time after the pulse which gave the closest approach between the local computed surface heat flux and the DNB heat flux according to Bernath. The axial distribution of the computed and critical heat fluxes for each of the three cases at the time of closest approach is given in Figures 4-11 thru 4-13. If the minimum approach to DNB is corrected to TRIGA Mark F conditions and cross-plotted, an estimate of the effective gap conductance of 450 Btu/hr-ft$^2$-°F is obtained for incipient burnout so that the case using 500 is thought to be representative of standard TRIGA fuel.

The surface heat flux at the midplane of the element is shown in Figure 4-14 with gap conductance as a parameter. It may be observed that the maximum heat flux is approximately proportional to the heat transfer coefficient of the gap, and the time lag after the pulse for which the peak occurs is also increased by about the same factor. The closest approach to DNB in these calculations did not necessarily occur at these times and places, however, as indicated on the curves of Figures 4-11 thru 4-13. The initial DNB point occurred near the core outlet for a local heat flux of about 340 kBtu/hr-ft$^2$-°F according to the more conservative Bernath correlations at a local water temperature approaching saturation.

This analysis indicates that after operation of the reactor at steady-state power levels of 1 MW(t), or after pulsing to equivalent fuel temperatures, the heat flux through the clad is reduced and therefore reduces the likelihood of reaching a regime where there is a departure from nucleate boiling. From the foregoing analysis, a maximum temperature for the clad during a pulse which gives a peak adiabatic fuel temperature of 1000°C is conservatively estimated to be 470°C.

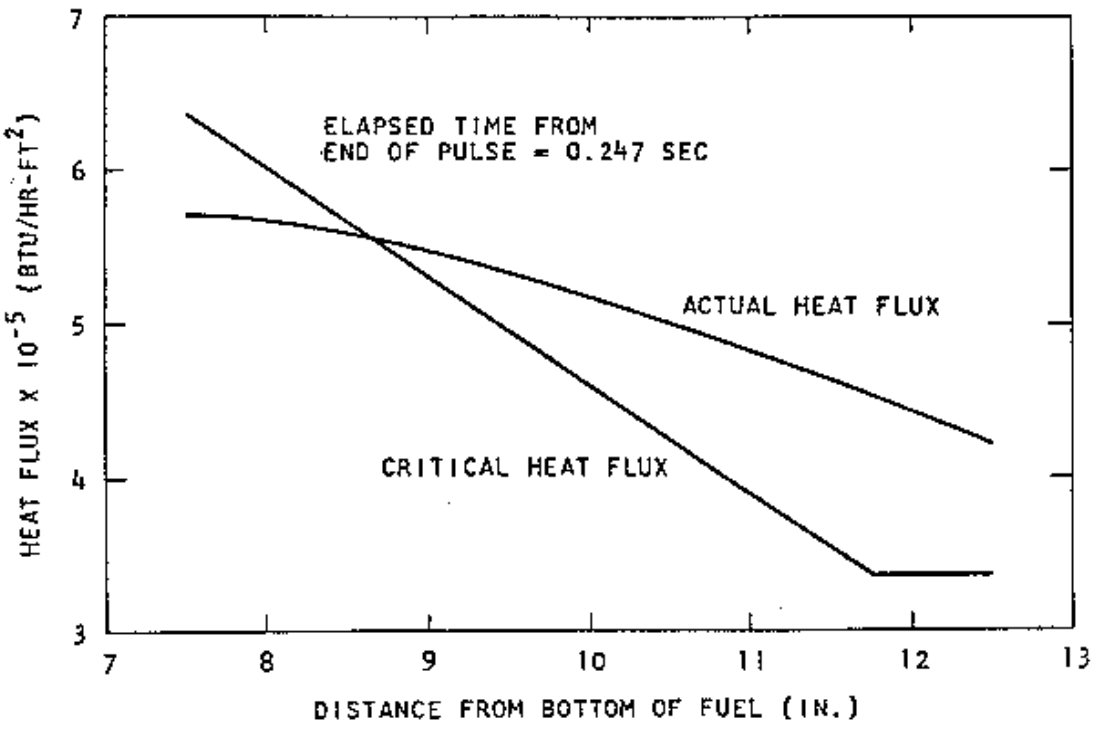


SURFACE HEAT FLUX DISTRIBUTION FOR STANDARD NON-GAPPED ($h_{gap}$=500) FUEL ELEMENT AFTER A PULSE

Figure 4-11

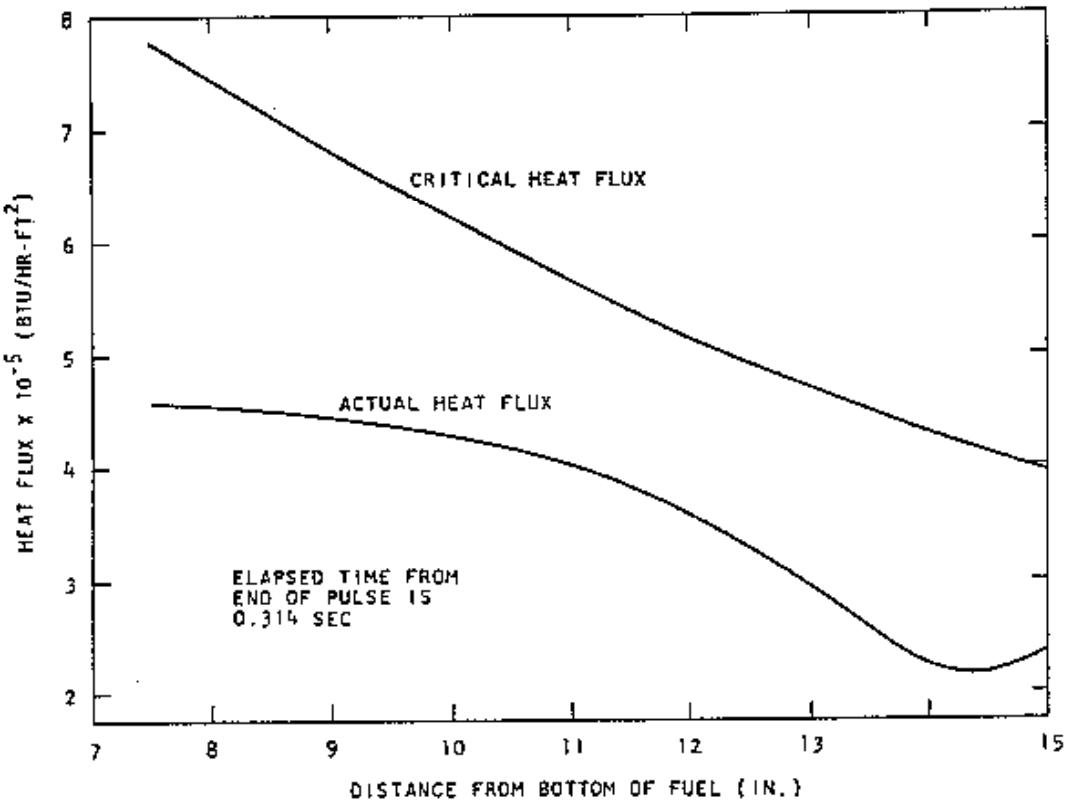


SURFACE HEAT FLUX DISTRIBUTION FOR STANDARD
NON-GAPPED ($h_{gap}$=375) FUEL ELEMENT AFTER A PULSE

Figure 4-12

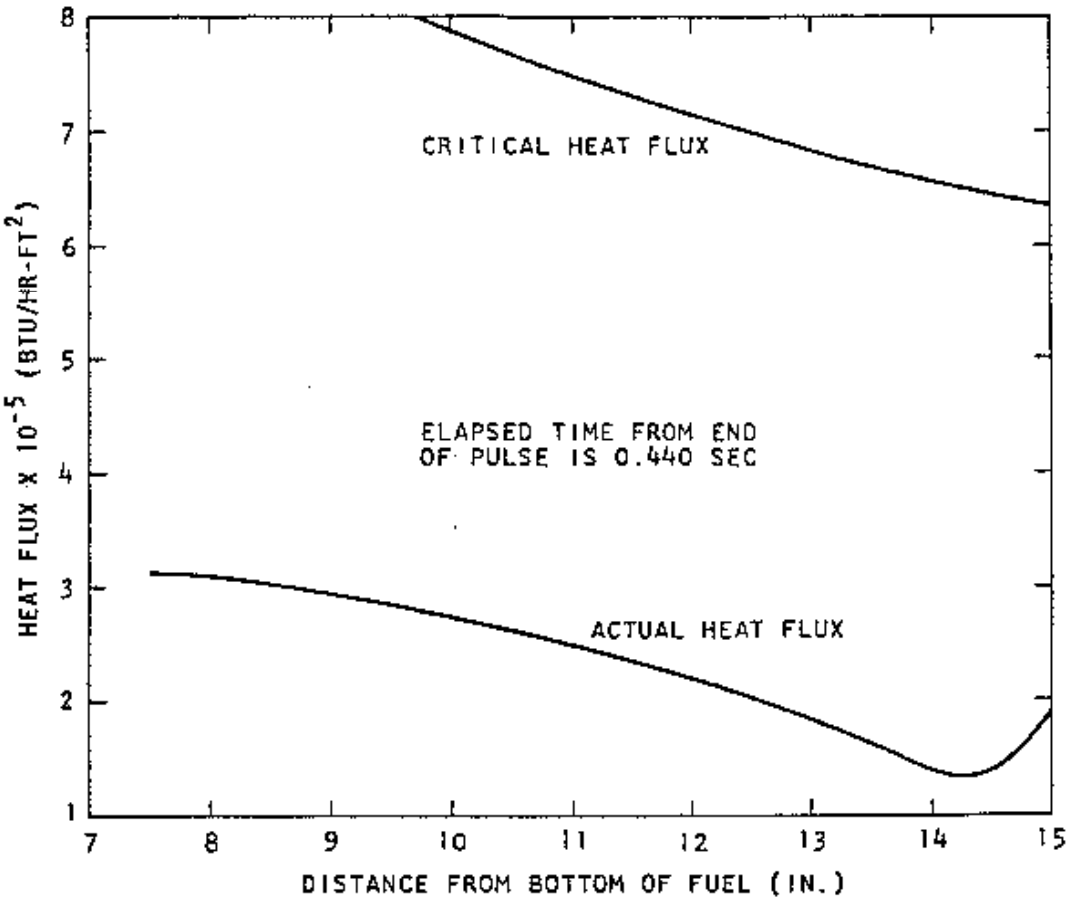


SURFACE HEAT FLUX DISTRIBUTION FOR STANDARD
NON-GAPPED ($h_{gap}$=250) FUEL ELEMENT AFTER A PULSE

Figure 4-13

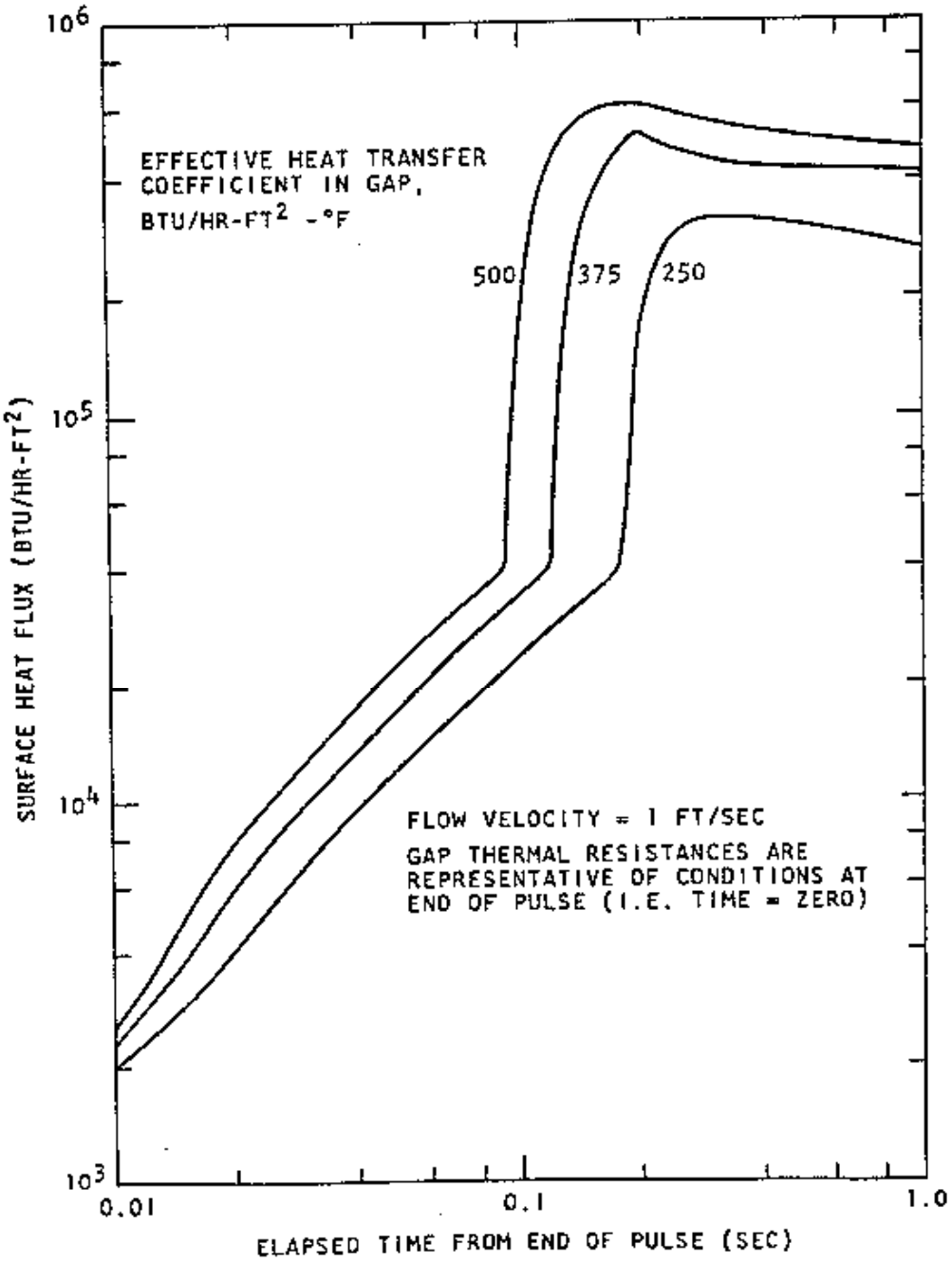


SURFACE HEAT FLUX AT MIDPOINT VERSUS TIME
FOR STANDARD NON-GAPPED FUEL ELEMENT AFTER A PULSE

Figure 4-14

As can be seen from Figure 4-3, the ultimate strength of the clad at a temperature of 470°C is 59,000 psi. If the stress produced by the hydrogen over pressure in the can is less than 59,000 psi, the fuel element will not undergo loss of containment. Referring to Figure 4-4, and considering U-ZrH fuel with a peak temperature of 1000°C, one finds the stress on the clad to be 12,600 psi. Further studies show that the hydrogen pressure which would result from a transient for which the peak fuel temperature is 1150°C would not produce a stress in the clad in excess of its ultimate strength. TRIGA fuel with a hydrogen to zirconium ratio of at least 1.65 has been pulsed to temperatures of about 1150°C without damage to the clad [16].

4.1.1.2 Finite Diffusion Rate. To assess the effect of the finite diffusion rate and the rehydriding at the cooler surfaces, the following analysis is presented.

As hydrogen is released from the hot fuel regions, it is taken up in the cooler regions and the equilibrium that is obtained is characteristic of some temperature lower than the maximum. To evaluate this reduced pressure, we will use diffusion theory to calculate the rate at which hydrogen is evolved and reabsorbed at the fuel surface.

Ordinary diffusion theory provides an expression for describing the time dependent loss of gas from a cylinder:

$$\frac{\bar{c} - c_f}{c_i - c_f} = \sum_{n=1}^{\infty} -\frac{4}{\xi_n^2} \exp -\left[\frac{\xi_n^2 \, Dt}{r_0^2}\right] , \qquad (3)$$

where

$c_i$, $c_f$, $\bar{c}$, = the average, the initial, and the final gas concentration in the cylinder, respectively,

$\xi_n$ = the roots of the Equation $J_0(x) = 0$,

D = the diffusion coefficient for the gas in the cylinder,

$r_0$ = the radius of the cylinder,

t = time.

Setting the term on the right-hand side of Equation 3 equal to $\kappa$, one can rewrite Equation 3 as:

$$\bar{c}/c_i = c_f/c_i + (1 - c_f/c_i)\,\kappa \quad , \qquad (4)$$

and the derivative in time is given by

$$\frac{d(\bar{c}/c_i)}{dt} = (1 - c_f/c_i)\,\frac{d\kappa}{dt} \quad . \qquad (5)$$

This represents the fractional release rate of hydrogen from the cylinder, f(t). The derivative of the series in the right-hand side of Equation 3 was approximated by

$$\frac{d\kappa}{dt} = -(7.339e^{-8.34\epsilon} + 29.88e^{-249\epsilon})\frac{d\epsilon}{dt} , \quad (6)$$

where $\epsilon = Dt/r_0^2$.

The diffusion coefficient for hydrogen in zirconium hydride in which the H/Zr ratio is between 1.56 and 1.86 is given by

$$D = 0.25\ e^{-17800/R(T+273)} , \quad (7)$$

where R = the gas constant and,

T = the zirconium hydride temperature in °C.

Equation 3 describes the escape of gas from a cylinder through diffusion until some final concentration is achieved. Actually, in the closed system considered here, not only does the hydrogen diffuse into the fuel-clad gap, but also it diffuses back into the fuel in the regions of lower fuel temperature. The gas also diffuses through the clad at a rate dependent on the clad temperature. Although this tends to reduce the hydrogen pressure, it is not considered in this analysis. When the diffusion rates are equal, an equilibrium condition will exist. To account for this, Equation 5 was modified by substituting for the concentration ratios the ratio of the hydrogen pressure in the gap to the equilibrium hydrogen pressure, $P_h/P_e$. Thus,

$$f(t) = \frac{d(\bar{c}/c_i)}{dt} = (1 - P_h(t)/P_e)\frac{d\kappa}{dt} \quad (8)$$

where $P_h(t)$ = the hydrogen pressure, a function of time and

$P_e$ = the equilibrium hydrogen pressure over the zirconium hydride which is a function of the fuel temperature.

The rate of change of the internal hydrogen pressure, in psi, inside the fuel element cladding is

$$\frac{dP_h}{dt} = \frac{14.7\ f(t)\ N_h}{6.02 \times 10^{23}}\ \frac{22.4}{V_g}\ \frac{T+273}{273} , \quad (9)$$

where $N_h$ = the number of molecules of $H_2$ in the fuel,

T = the gas temperature (°C),
f(t) = the fractional loss rate from Equation 8,
$V_g$ = the free volume inside the fuel clad (liters).

As the atom density of hydrogen in ZrH (H/Zr ; 1.65) is about 0.1 moles and the fuel volume is 400 cubic cm., $N_h$ is 19.9 moles ($H_2$). The free volume is assumed to consist of a cylindrical volume, at the top of the element, 1/8-in. high with a diameter of 1.43 in. for a total of 3.3 cubic cm. Also, the temperature of the hydrogen in the gap was assumed to be the temperature of the clad. The effect of changing these two assumptions was tested by calculations in which the gap volume was decreased by 90% and the temperature of the hydrogen in the gap was set up equal to the maximum fuel temperature. Neither of these changes resulted in maximum pressures different from those based on the original assumptions although the initial rate of pressure increase was greater. For these conditions

$$P_h = 7.29 \times 10^3 \, (T + 273) \int f(t) \, dt \, . \qquad (10)$$

The fuel temperature used in Equation 7 to evaluate the diffusion coefficient is expressed as

$$T(z) = T_0 \quad ; \; t < 0 \quad ,$$
$$T(z) = T_0 + (T_m - T_0) \cos [2.45(z-0.5)] \quad ; \; t \geq 0 \quad , \qquad (11)$$

where $T_m$ = the peak fuel temperature (°C),

$T_0$ = the clad temperature (°C),

z = the axial distance expressed as a fraction of the fuel length,

t = the time after step increase in power.

It was assumed that the fuel temperature was invariant with radius. The hydrogen pressure over the zirconium hydride surface when equilibrium prevails is strongly temperature dependent as shown in Figure 4-2 and, for ZrH (H/Zr ; 1.65), can be expressed by

$$P_e = 2.07 \times 10^9 \, e^{-1.974 \times 10^4/(T+273)} \, . \qquad (12)$$

The coefficients have been derived from data developed by Johnson. The rate at which hydrogen is released or reabsorbed takes the form

$$g(t,z) = \frac{[P_e(z) - P_h(t)]}{P_e(z)} \, f(t,z) \quad , \qquad (13)$$

where f(t,z) = the derivative given in Equation 8 with respect to time evaluated at the axial position z,
$P_h(t)$ = the hydrogen pressure in the gap at time t,
$P_e(z)$ = the equilibrium hydrogen pressure at the ZrH temperature at position z.

The internal hydrogen pressure is then

$$P_h(t) = 7.29 \times 10^3 \, (T_0 + 273) \int_0^t \int_0^1 g(t,z) \, dz \, dt \, . \qquad (14)$$

This Equation was approximated by

$$P_h(t_i) = 7.29 \times 10^3 \, (T_0 + 273) \times \sum_{i=1}^{n} \sum_{j=1}^{m} \left[ 1 - \frac{P_H(t_{i-1})}{P_E(z_j)} \right] \times f(t_i, z_j) \, \delta z \, \delta t \, , \qquad (15)$$

where the internal summation is over the fuel element length increments and the external summation is over time.

For the case in which the maximum fuel temperature is 1150°C, the equilibrium hydrogen pressure in ZrH (H/Zr ; 1.65) is 2000 psi. Calculations indicate, however, that the internal pressure increases to a peak at about 0.3 sec, at which time the pressure is about one-fifth of the equilibrium value or abut 400 psi. After this time, the pressure slowly decreases as the hydrogen continues to be redistributed along the length of the element from the hot regions to the cooler regions.

Calculations have also been made for step increases in power to peak fuel temperatures greater than 1150°C. Over a 200°C range, the time to the peak pressure and the fraction of the equilibrium pressure value achieved were approximately the same as for the 1150°C case. Thus, if the clad remains below about 500°C, the internal pressure that would produce the yield stress in the clad (35,000 psi) is about 1000 psi and the corresponding equilibrium hydrogen pressure corresponds to a maximum fuel temperature of about 1250°C in ZrH (H/Zr ; 1.65). Similarly, an internal pressure of 1600 psi would produce a stress equal to the ultimate clad strength (over 59,000 psi). This corresponds to an equilibrium hydrogen pressure of 5 x 1600 or 8000 psi and a fuel temperature of about 1300°C.

Measurements of hydrogen pressure in TRIGA fuel elements during steady-state operation have not been made. However, measurements have been made during transient operations and compared with the results of an analysis similar to that described here. These measurements indicated that in a pulse in which the maximum temperature in the fuel was greater than 1000°C the maximum pressure was only about 6% of the equilibrium value evaluated at the peak temperature. Calculations of the pressure resulting from such a pulse using the methods described above gave calculated pressure values about three times greater than the measured values.

An instantaneous increase in fuel temperature will produce the most severe pressure conditions. When a peak fuel temperature of 1150°C is reached by increasing the power over a finite period of time, the resulting pressure will be no greater than that for the step change in

power analyzed above. As the temperature rise times become long compared with the diffusion time of hydrogen, the pressure will become increasingly less than for the case of a step change in power. The reason for this is that the pressure in the clad element results from the hot fuel dehydriding faster than the cooler fuel rehydrides (takes up the excess hydrogen to reach an equilibrium with the hydrogen over pressure in the can). The slower the rise to peak temperature, the lower the pressure because of the additional time available for rehydriding.

4.1.1.3 Summary The foregoing analysis gives a strong indication that the clad will not be ruptured if fuel temperatures are never greater than in the range of 1200°C to 1250°C, providing that the clad temperature is less than about 500°C. However, a conservative safety limit of 1150°C has been chosen for this condition. As a result, at this safety limit temperature the pressure is about a factor of 4 lower than would be necessary for clad failure. This factor of 4 is more than adequate to account for uncertainties in clad strength and manufacturing tolerances.

Under any condition in which the clad temperature increases above 500°C, the temperature safety limit must be decreased as the clad material loses strength at elevated temperatures. To establish this limit, it is assumed that the fuel and the clad are at the same temperature. There are no conceivable circumstances that could give rise to a situation in which the clad temperatures was higher than the fuel temperature.

In Figure 4-4 there is plotted the stress imposed on the clad by the equilibrium hydrogen pressure as a function of the fuel temperature, again assuming a clad radius of 0.73 in. and a thickness of 0.02 in. Also shown is the ultimate strength of 304 stainless steel at the same temperatures. The use of these data for establishing the safety limit is justified as

a. the method used to measure ultimate strength requires the imposition of the stress over a longer time than would be imposed for accident conditions,

b. the stress is not applied biaxially in the ultimate strength measurements as it is in the fuel clad.

The point at which the two curves in Figure 4-4 intersect is the safety limit, that is, 970°C. At that temperature the equilibrium hydrogen pressure would impose a stress on the clad equal to the ultimate strength of the clad.

The same argument about the redistribution of the hydrogen within the fuel presented earlier is valid for this case also. In addition, at elevated temperatures the clad becomes quite permeable to hydrogen. Thus, not only will hydrogen redistribute itself within the fuel to reduce the pressure, but also some hydrogen will escape from the system entirely.

The use of the ultimate strength of the clad material in the establishment of the safety limit under these conditions is justified because of the transient nature of such accidents. Although the high clad temperatures imply sharply reduced heat transfer rates to the surroundings (and consequently longer cooling times), only slight reductions in the fuel temperature are necessary to reduce the stress sharply. A 50°C decrease in temperature from 970°C to 920°C will reduce the stress by a factor of 2.

As a safety limit, the peak adiabatic fuel temperature to be allowed during transient conditions is considered to be 1150°C for U-$ZrH_{1.65}$.

4.1.2. Prompt Negative Temperature Coefficient

The basic parameter which allows the TRIGA reactor system to operate safely with large step insertions of reactivity is the prompt negative temperature coefficient associated with the TRIGA fuel and core design. This temperature coefficient ($\alpha$) also allows a greater freedom in steady-state operation as the effect of accidental reactivity changes occurring from the experimental devices in the core is greatly reduced.

GA Technologies, the designer of the reactor, has developed techniques to calculate the temperature coefficient accurately and therefore predict the transient behavior of the reactor. This temperature coefficient arises primarily from a change in the disadvantage factor resulting from the heating of the uranium zirconium hydride fuel-moderator elements. The coefficient is prompt because the fuel is intimately mixed with a large portion of the moderator and thus fuel and solid moderator temperatures rise simultaneously. A quantitative calculation of the temperature coefficient requires a knowledge of the energy dependent distribution of thermal neutron flux in the reactor.

The basic physical processes which occur when the fuel-moderator elements are heated can be described as follows: the rise in temperature of the hydride increases the probability that a thermal neutron in the fuel element will gain energy from an excited state of an oscillating hydrogen atom in the lattice. As the neutrons gain energy from the ZrH, their mean free path is increased appreciably. This is shown qualitatively in Figure 4-15. Since the average chord length in the fuel element is comparable with a mean free path, the probability of escape from the fuel element before capture is increased. In the water the neutrons are rapidly rethermalized so that the capture and escape probabilities are relatively insensitive to the energy with which the neutron enters the water. The heating of the moderator mixed with the fuel thus causes the spectrum to harden more in the fuel than in the water. As a result, there is a temperature dependent disadvantage factor for the unit cell in the core which decreases the ratio of absorptions in the fuel to total cell absorptions as the fuel element temperature is increased. This brings about a shift in the core neutron balance, giving a loss of reactivity.

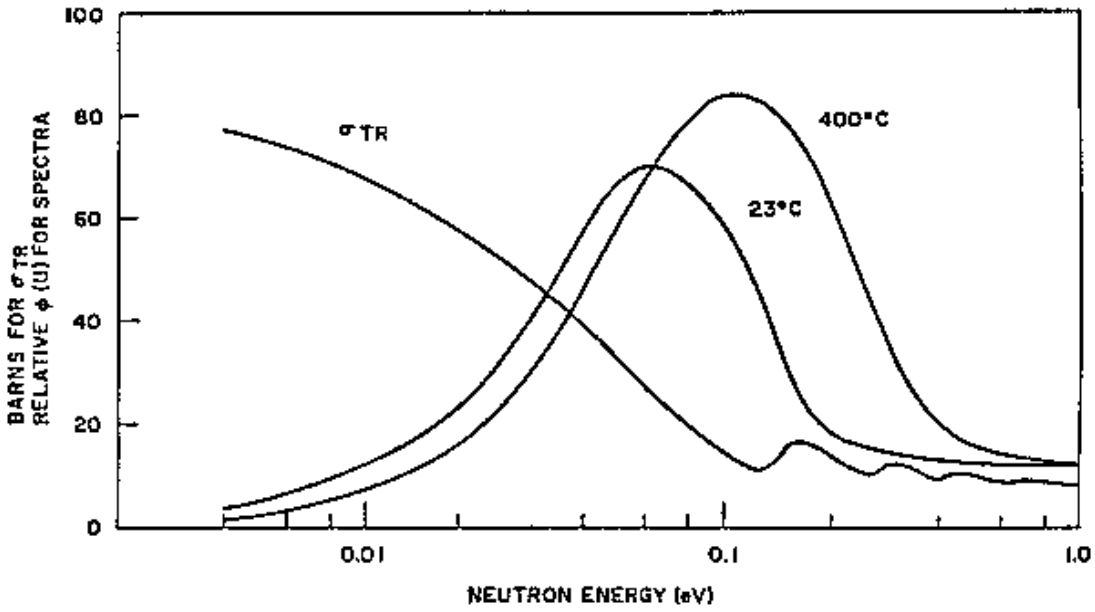


TRANSPORT CROSS SECTION FOR HYDROGEN
IN ZrH AND AVERAGE NEUTRON SPECTRA IN FUEL ELEMENT

Figure 4-15

The temperature coefficient then, depends on spatial variations of the thermal neutron spectrum over distances of the order of a mean free path with large changes of mean free path occurring because of the energy change in a single collision. A quantitative description of these processes requires a knowledge of the differential slow neutron energy transfer cross section in water and zirconium hydride, the energy dependence of the transport cross section of hydrogen as bound in water and zirconium hydride, the energy dependence of the capture and fission cross sections of all relevant materials, and a multigroup transport theory reactor description which allows for the coupling of groups by speeding up as well as by slowing down.

4.1.2.1. Codes Used for Calculations. Calculational work on the temperature coefficient made use of a group of codes developed by GA Technologies: GGC-3 [17], GAZE-2 [18], and GAMBLE-5 [19], as well as DTF-IV [20], an $S_n$ multigroup transport code written at Los Alamos. Neutron cross sections for energies above thermal ($\geq$1 eV) were generated by the GGC-3 code. In this code, fine group cross sections (~100 groups), stored on tape for all commonly used isotopes, are averaged over a space independent flux derived by solution of the $B_1$ equations for each discrete reactor region composition. This code and its related cross-section library predict the age of each of the common moderating materials to within a few percent of the experimentally determined values and use the resonance integral work of Adler, Hinman, and Nordheim [21] to generate cross sections for resonance materials which are properly averaged over the region spectrum.

Thermal cross sections were obtained in essentially the same manner using the GGC-3 code. However, scattering kernels were used to describe properly the interactions of the neutrons with the chemically bound moderator atoms. The bound hydrogen kernels used for hydrogen in the water were generated by the THERMIDOR code [22] using thermalization work of Nelkin [23]. Early thermalization work by McReynolds et al [24] on zirconium hydride has been greatly extended at GA Technologies [25], and work by Parks resulted in the SUMMIT [26] code, which was used to generate the kernels for hydrogen as bound in ZrH. These scattering models have been used to predict adequately the water and hydride (temperature dependent) spectra as measured at the GA Technologies linear accelerator as shown in Figure 4-16 and Figure 4-17 [27].

4.1.2.2. ZrH Model. Qualitatively, the scattering of slow neutrons by zirconium hydride can be described by a model in which the hydrogen atom motion is treated as an isotropic harmonic oscillator with energy transfer quantized in multiples of ~0.14 eV. More precisely, the SUMMIT model uses a frequency spectrum with two branches, one for the optical modes for energy transfer with the bound proton, and the other for the acoustical modes for energy transfer with the lattice as a whole. The optical modes are represented as a broad frequency band centered at 0.14 eV, and whose width is adjusted to fit the cross section data of Woods et al. [28]. The low frequency acoustical modes are assumed to have a Debye spectrum with a cutoff of 0.02 eV and a weight determined by an effective mass of 360.

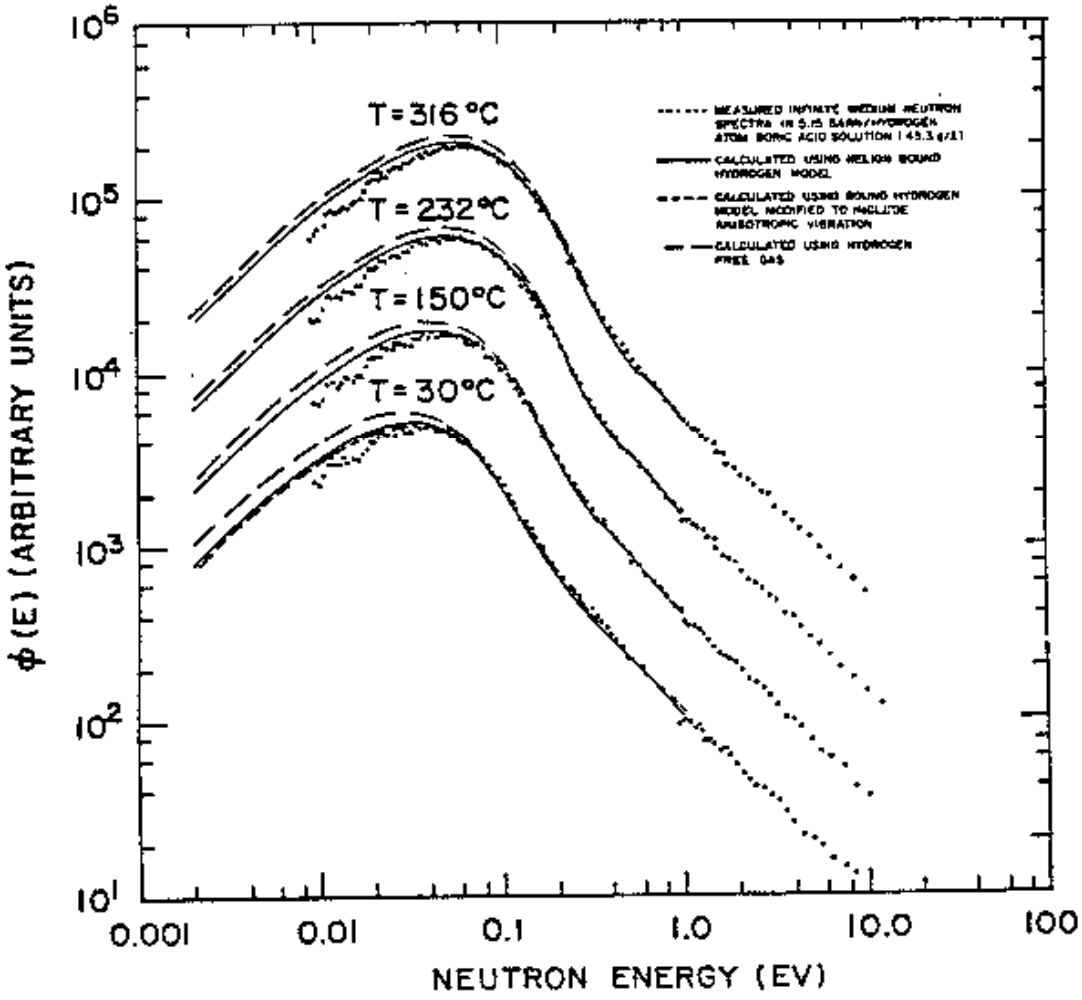


A COMPARISON OF NEUTRON SPECTRA
BETWEEN EXPERIMENTS AND SEVERAL HYDROGEN MODELS

Figure 4-16

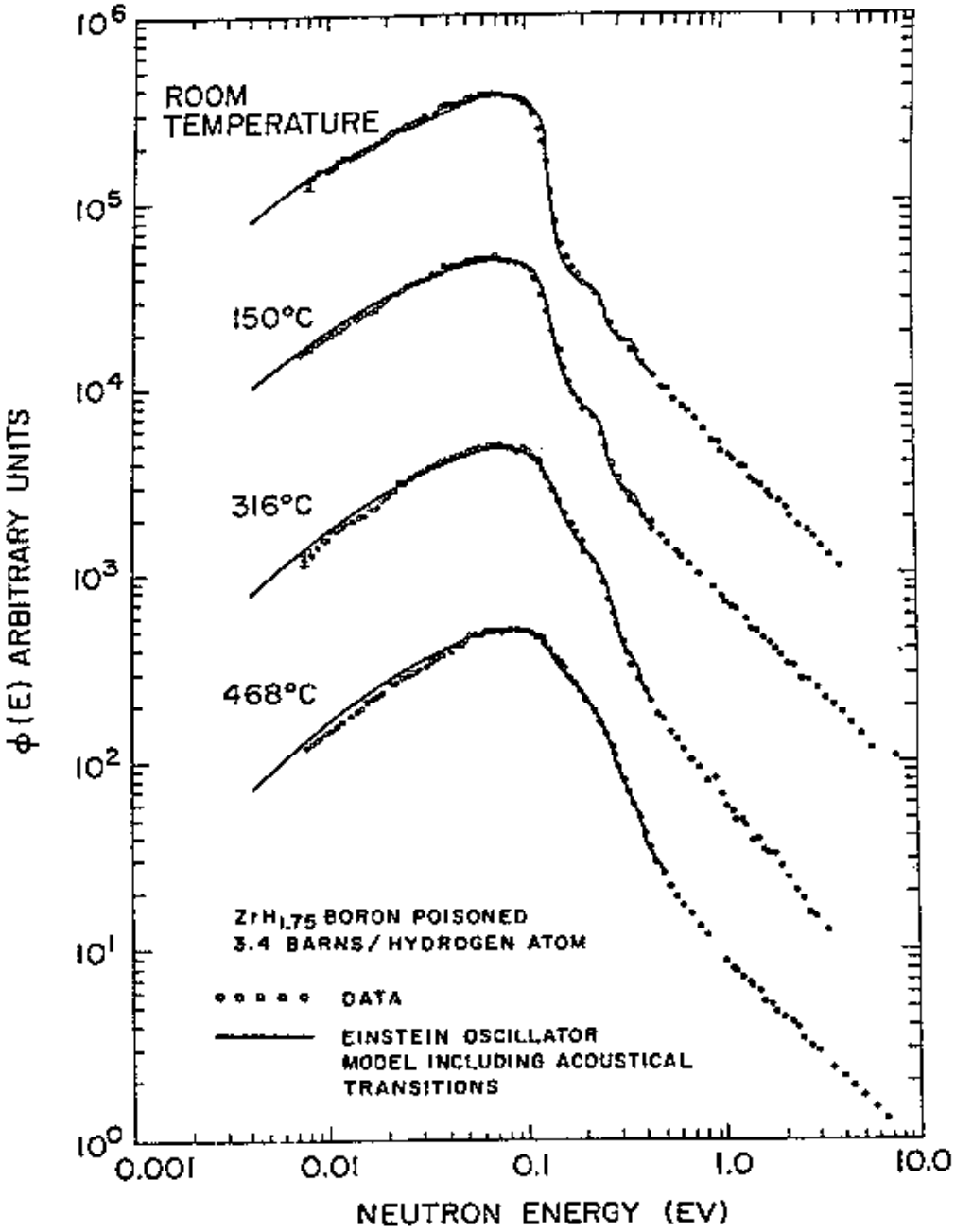


EFFECT OF TEMPERATURE VARIATION ON
ZIRCONIUM HYDRIDE NEUTRON SPECTRA

Figure 4-17

This structure then allows a neutron to slow down by the transition in energy units of ~0.14 eV as long as its energy is above 0.14 eV. Below 0.14 eV the neutron can still lose energy by the inefficient process of exciting acoustic Debye type modes in which the hydrogen atoms move in phase with the zirconium atoms, which in turn move in phase with one another. These modes therefore, correspond to the motion of a group of atoms whose mass is much greater than that of hydrogen, and indeed even greater than the mass of zirconium. Because of the large effective mass, these modes are very inefficient for thermalizing neutrons, but for neutron energies below 0.14 eV they provide the only mechanism for neutron slowing down within the ZrH. (In a TRIGA core, the water also provides for neutron thermalization below 0.14 eV.) In addition, in the ZrH it is possible for a neutron to gain one or more energy units of ~0.14 eV in one or several scatterings, from excited Einstein oscillators. Since the number of excited oscillators present in a ZrH lattice increases with temperature, this process of neutron speeding up is strongly temperature dependent and plays an important role in the behavior of ZrH moderated reactors.

4.1.2.3. Calculations. Calculations of the temperature coefficient were done in the following steps:

a. Multigroup cross sections were generated by the GGC-3 code for a homogenized unit cell. Separate cross-section sets were generated for each fuel element temperature by use of the temperature dependent hydride kernels and Doppler broadening of the U-238 resonance integral to reflect the proper temperature. Water at room temperature was used for all prompt coefficent calculations.

b. A value for $k_\infty$ was computed for each fuel element temperature by transport cell calculations, using the $P_1$ approximation. Comparisons have shown $S_4$ and $S_8$ results to be nearly identical. Group dependent disadvantage factors were calculated for each cell region (fuel, clad, and water) where the disadvantage factor is defined as the ratio: $\Phi_g^r$ / $\Phi_g^c$ (region/cell).

c. The thermal group disadvantage factors were used as input for a second GGC-3 calculation where cross sections for a homogenized core were generated which gave the same neutron balance as the thermal group portion of the discrete cell calculation.

d. The cross sections for an equivalent homogenized core were used in a full reactor calculation to determine the contribution to the temperature coefficient due to the increased leakage of thermal neutrons into the reflector with increasing hydride temperature. This calculation still requires several thermal groups, but transport effects are no longer of major concern. Thus, reactivity calculations as a function of fuel element temperature have been done on the entire reactor with the use of diffusion theory codes.

Results from the above calculations indicate that more than 50% of the temperature coefficient for a standard TRIGA core comes from the temperature-dependent disadvantage factor or "cell effect", and ~20% each from Doppler broadening of the U-238 resonances and temperature dependent leakage from the core. These effects produce a temperature coefficient of ~ -0.01%/°C, which is rather constant with temperature. The temperature coefficient is shown in Figure 4-18 for the high-hydride core of this TRIGA.

4.1.3. Steady-State Reactor Power

The following evaluation has been made for a TRIGA system operating with cooling from natural convection flow around the fuel elements. This analysis investigates the limits to which such a system may be operated.

The analysis was conducted by considering the hydraulic characteristics of the flow channel from which the heat rejection rate is maximum. The geometrical data from this channel are given in Table 4-2. All symbols in Equation 16 through 45 are defined in the list of nomenclature in Section 4.1.3.9.

Table 4-2

HYDRAULIC FLOW PARAMETERS

| | |
|---|---|
| Flow area ($ft^2$/element) | 0.00580 |
| Wetted perimeter (ft/element) | 0.3861 |
| Hydraulic diameter (ft) | 0.0601 |
| Fuel element diameter (ft) | 0.1229 |
| Fuel surface area ($ft^2$) | 0.4826 |

The heat generation rate in the fuel element is distributed axially in a cosine distribution chopped at the end such that the peak-to-average ratio is 1.25. The number of fuel elements in the core is assumed for 1 MW operation, but the departure from nucleate boiling (DNB) ratio is conservatively evaluated on the basis of 85 elements.

The driving force is supplied by the buoyance of the heated water in the core. Countering this force are the contraction and expansion losses at the entrance and exits to the channel, and the acceleration and potential energy losses and friction losses in the cooling channel itself.

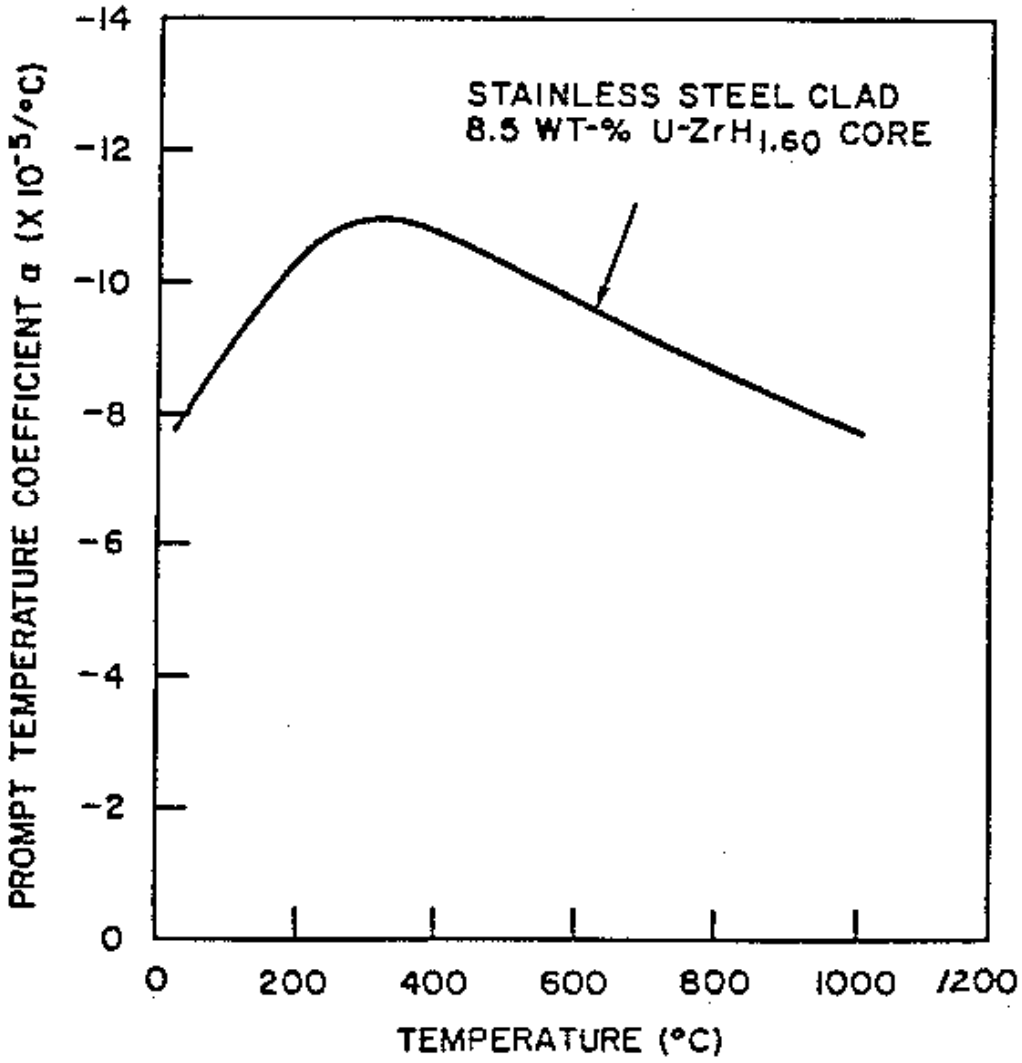


PROMPT NEGATIVE TEMPERATURE COEFFICIENT
VERSUS AVERAGE FUEL TEMPERATURE FOR TRIGA

Figure 4-18

Figure 4-19 illustrates schematically the natural convection system established by the fuel elements bounding one flow channel in the core. The system shown is general and does not represent any specific configuration. Steady-state flow is governed by the Equation

$$\delta p_i + \delta p_e + \delta p_l + \delta p_u + \sum_{j=1}^{n} \delta p_j = z_t/v_o \quad , \qquad (16)$$

where the left-hand member represents the pressure drops through the flow channel due to entrance, exit, friction, acceleration, and gravity losses and the right-hand member represents the driving pressure due to the static head in the pool. The pressure drops through the flow channel are dependent on the flow rate while the available static driving pressure is fixed for a known core height and pool temperature. The analysis, therefore, becomes an iterative one in which the left-hand side of Equation 16 is evaluated on the basis of an assumed flow rate and compared with the known right-hand side until equality is achieved. The method has been programmed for digital computer solution. The methods of evaluating each of the $\delta p$ terms in Equation 16 for known power distribution and flow geometry and assumed flow rates are discussed below.

4.1.3.1. Entrance Loss, $\delta p_i$.

The entrance loss, $\delta p_i$, may be evaluated in the usual way as a fraction of the velocity head in the lower grid plate hole:

$$\delta p_i = \frac{( k_{i_1} + k_{i_2} ) \ v_o}{2g \ A_i^2} \ (NW)^2 \quad , \qquad (17)$$

where N = the number of channels which receive their flow from a single hole in the lower grid plate,

$k_{i_1}$ = the loss factor for the entrance to the hole in the lower grid plate. For even slight rounding of the entrance, $k_{i_1}$ will be no greater than 0.30,

$k_{i_2}$ = the loss factor covering transfer of the flow from the hole in the lower grid plate to the coolant channels. In most cases this can be satisfactorily approximated as a sudden expansion using $k_{i_2} = 1.0$.

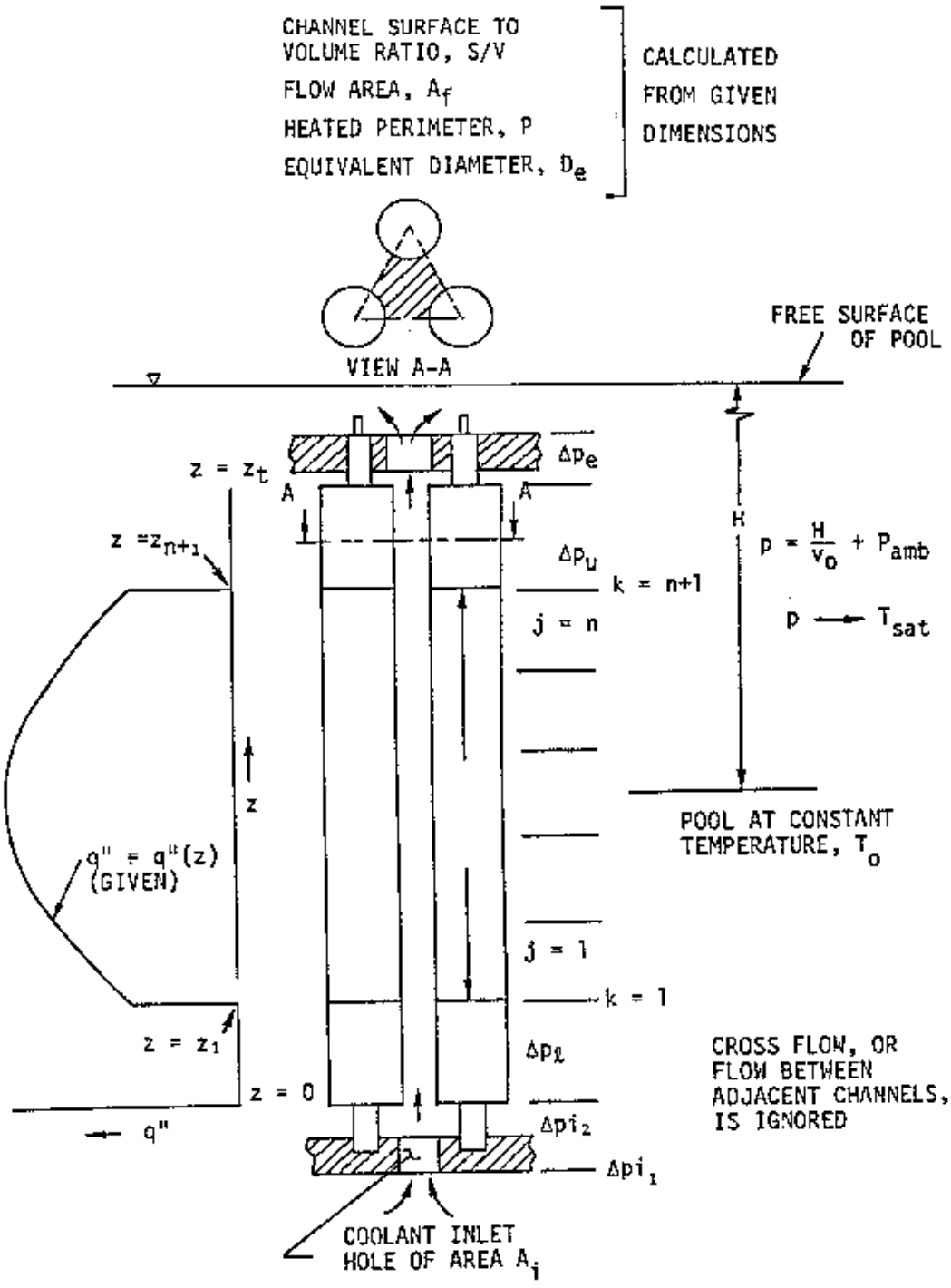


GENERAL FUEL ELEMENT CONFIGURATION FOR SINGLE COOLANT CHANNEL IN THE TRIGA

Figure 4-19

4.1.3.2. Exit Loss, $\delta p_e$.

The exit loss is expressed in terms of a coefficient $K_e$ which is the fraction of the velocity head in the flow channel which is not recovered:

$$\delta p_e = \frac{K_e \, v_{n+1}}{2g A_f^2} \, W^2 \quad . \tag{18}$$

The term $v_{n+1}$ is the specific volume at the highest axial station along the heated length of the core. It is evaluated from the temperature $T_{n+1}$ which is obtained from an overall heat balance:

$$T_{n+1} = q_t/WC + T_o \, , \tag{19}$$

$$\text{where } q_t = P \int_{z_1}^{z_{n+1}} q''(z) \, dz \, .$$

4.1.3.3. Loss Through Portion of Channel Adjacent to Lower Reactor $\delta p_l$.

The flow is isothermal at the bulk pool temperature so that

$$\delta_{p_l} = \frac{f_m \, v_o \, \delta z_l}{2g \, D_e \, A_f^2} \, W^2 + \frac{\delta z_l}{v_o} \quad . \tag{20}$$

$f_m$ is evaluated from the Moody chart (assuming smooth surface) on the basis of a Reynolds number which is

$$R_e = \frac{D_e \, v_o}{A_f \, \nu_o} \, W \, . \tag{21}$$

4.1.3.4. Loss Through Portion of Channel Adjacent to Upper Reactor $\delta p_u$.

The flow is isothermal at $T_{n+1}$ where $T_{n+1}$ is determined by Equation 19 :

$$\delta P_u = \frac{f_m \, v_n \, \delta z_u}{2g \, D_e \, A_f^2} \, W^2 + \frac{\delta z_u}{v_n} \quad . \tag{22}$$

$f_m$ is again evaluated from the Moody chart, assuming smooth surface, on the basis of a Reynolds number which is

$$R_e = \frac{D_e \, v_n}{A_f \, \nu_n} \, W \quad . \tag{23}$$

4.1.3.5. Loss Through Each Increment of the Channel Adjacent to the Fueled Portion of the Elements, $\delta p_j$.

For the present, let us assume that the entire heated portion of the channel is in subcooled boiling. This implies that the wall temperatures calculated from subcooled boiling correlations are lower than those calculated for convection alone and that the liquid is below its saturation temperature at all locations. The pressure drop through an increment is given by

$$\delta p_{n-(n+1)} = \frac{v_{m_{k+1}} - v_{m_k}}{g A_f^2} W^2 + \frac{f_{b_j} v_{m_j} \delta z}{2g A_f^2 D_e} W^2 + \frac{\delta z}{v_{m_j}} \quad (24)$$

(acceleration) (friction) (gravity)

4.1.3.6. Acceleration Term.

$v_m$ denotes the mean specific volume and is larger than the liquid specific volume, because of the vapor voidage:

$$v_m = v/(1-\alpha) \quad . \quad (25)$$

$\alpha$ is the void fraction or the fraction of a channel cross section which is occupied by vapor. $\alpha$ may be calculated from the vapor volume (cubic in. vapor/square in. heating surface) and the flow channel geometry. Denoting the vapor volume as $\xi$,

$$\alpha = \xi \, (S/V) \quad (26)$$

where S/V is the surface to volume ratio of the coolant channel. The parameter $\xi$, is dependent on the surface heat flux, the subcooling of liquid and the velocity of the liquid. It can be evaluated only by experiment. Data given by Jordan and Leppert [29] were used to estimate $\xi$; these data are plotted in Figures 4-20 and 4-21. Most of this represents a flow velocity of 4 ft/sec and appears to be the only available data applicable under the thermal conditions encountered in TRIGA type reactors. Extrapolations from these data are made for flow velocities different from 4 ft/sec. The extrapolations were based on a small amount of data given for flow velocities other than 4 ft/sec. The liquid temperature at a station, $T_k$, may be calculated from

$$T_k = \frac{P \int_{z_1}^{z_k} q''(z) dZ}{WC} + T_o \quad . \quad (27)$$

Therefore, one finds $\xi$ (Figure 4-21) from $T_{sat} - T_k$ and $q_k''$, where $T_{sat}$ and $q_k''$ are known.

Since $\alpha_k = \xi_k \, (S/V)$

and $v_k$ is a function of $T_k$, $v_m$ may be evaluated from Equation 25.

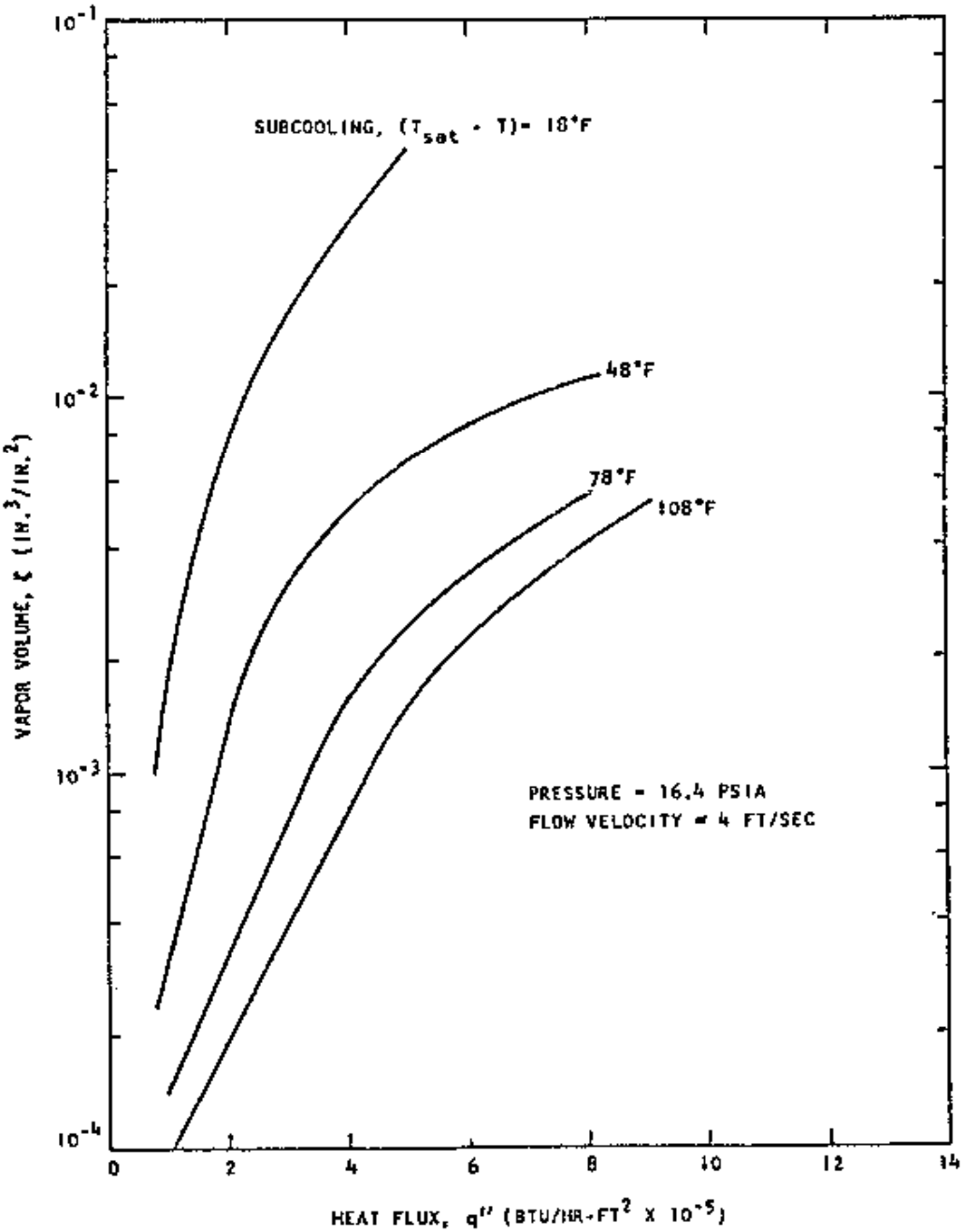


EXPERIMENTALLY DETERMINED VAPOR VOLUMES FOR
SUBCOOLED BOILING IN A NARROW VERTICAL ANNULUS

Figure 4-20

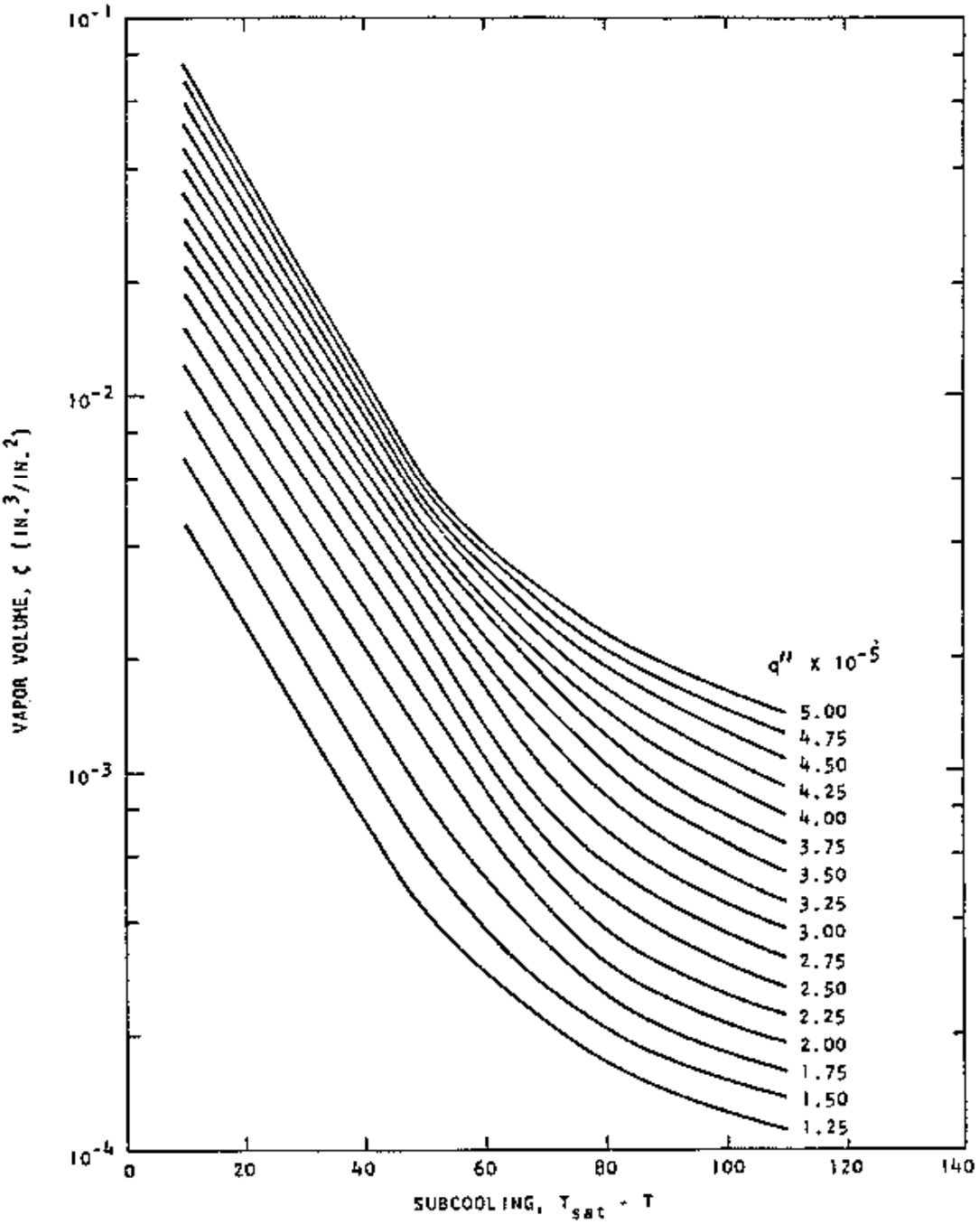


CROSS PLOT OF Figure 4-20 USED IN CALCULATIONS

Figure 4-21

4.1.3.7. Friction Term.

$v_{mj}$ denotes a linear average of the mean specific volumes at the upper and lower boundaries of an increment. The approximate mean value is assumed to apply over the entire increment so that

$$v_{m_j} = \frac{v_{m_k} + v_{m_{k+1}}}{2} \tag{28}$$

A friction factor $f_{bj}$ is applied locally to calculate the friction pressure drop over the increment in subcooled boiling. Jordan and Leppert develop the correlation

$$f_b = 8\, S_t = \frac{8\, h_b}{\rho\, CV} = \frac{8\, q''}{\rho\, CV\, (T_w - T)} \quad , \tag{29}$$

and provide experimental verification near atmospheric pressure in the range $0.0015 < S_t < 0.0050$. This is simply an extension of Reynolds' analogy to the case of subcooled boiling. The Equation of continuity is used to write Equation 29 as

$$f_b = \frac{8\, q''\, A_f}{WC\, (T_w - T)} \quad . \tag{30}$$

which may be evaluated if $T_w$ is known. For subcooled boiling, the heat transfer is usually defined by an experimentally determined correlation of $q''$ vs $(T_w - T_{sat})$ which has been obtained over a given range of flow velocity and pressure. McAdams [30] gives such a correlation for pressures between 2 and 6 atmospheres and flow velocities between 1 and 12 ft/sec. This correlation will be used to determine $T_w$ for use in Equation 30.

Approximate mean values are assumed to apply over the entire increment so that

$$f_{b_j} = 1/2\, \frac{8\, A_f}{WC} \left[ \frac{q''_k}{T_{w,k} - T_k} + \frac{q''_{k+1}}{T_{w,k+1} - T_{k+1}} \right] \quad , \tag{31}$$

and $$T_w - T_{sat_j} = \frac{\phi(q''_k) + \phi(q''_{k+1})}{2} \quad ,$$

where $\phi(q'')$ is the correlation of McAdams previously cited.

4.1.3.8. Gravity Term.

The gravity term is evaluated from $v_j$ calculated from Equation 28.

As implied in Section 4.1.3.5., each increment must be checked to determine whether heat is being transferred by subcooled boiling or by convection. $T_w$ is evaluated at the lower boundary of the increment on the basis of both the correlation from McAdams for subcooled boiling and a standard correlation for convection (Dittus-Boelter). If the $T_w$ calculated from convection correlations is less than that obtained for subcooled boiling, boiling is assumed not to be present in the increment. Equation 24 still applies, but since there is no boiling and hence no vapor void, $v_m$ becomes v and $f_b$ becomes $f_m$.

In the foregoing analysis an assumption was made that all of the vapor formed on the surface of the fuel element detaches and adds to the fluid buoyancy. This is not a conservative assumption. The position where vapor bubbles first leave the heated surface is obtained from two considerations; first, the balance of the forces exerted on the vapor bubble while it is in contact with the wall (buoyancy, surface tension, and friction), and, second, the temperature distribution in the single phase liquid away from the walls.

Determination of the buoyance forces resulting from the formation and subsequent detachment of vapor bubbles is complicated by the difficulty in predicting the point at which the vapor detaches, and the fraction of that vapor which subsequently condenses. The problem was simplified by making use of an analysis performed by Levy [31] to determine the position at which the vapor detaches from the wall, assuming that at that point all of the vapor detaches and, finally, that there is no recombination of the vapor with subcooled fluid.

According to Levy the position at which the vapor leaves the surface is obtained from considering the balance of forces exerted on the vapor bubble while it is in contact with the wall, and the temperature distribution in the single phase liquid away from the wall.

The forces acting on the bubble in the vertical direction consist of a buoyant force, $F_B$; a frictional force, $F_F$, exerted by the liquid on the bubble; and a surface tension force, $F_S$, vertical component.

The buoyant force, $F_B$, is given by

$$F_B = \frac{C_B\, r_B^3\, (\rho_L - \rho_v) g}{g_c} , \qquad (32)$$

where $r_B$ is the bubble radius, $C_B$ is a proportionality constant, $\rho_L$ and $\rho_v$ are the liquid and vapor density, g is the acceleration due to gravity and $g_c$ is a conversion ratio from lb-force to lb-mass. The frictional force, $F_F$, is related to the liquid frictional pressure drop per unit length, $(-dp/dz)_F$. The pressure differential across the bubble is proportional to the pressure differential times the bubble radius and it acts across an area proportional to the square of the bubble radius.

Relating the pressure differential to the wall shear stress $\tau_w$ by

$$-(dp/dz)_F = 4\,\tau_w/D_H \quad , \tag{33}$$

there results for $F_F$:

$$F_F = C_F\,(\,\tau_w / D_H\,)\,r_B^3 \quad , \tag{34}$$

where $C_F$ is a constant of proportionality and $D_H$ is the hydraulic diameter (four times the cross-sectional area divided by the wetted perimeter). The surface tension force, $F_S$, is given by

$$F_S = C_S\,r_B\,\sigma \quad , \tag{35}$$

where $C_S$ is a proportionality constant and $\sigma$ is the surface tension. Assuming upward flow the balance of these forces results in the following solutions for the bubble radius:

$$r_B = \left[ \frac{C_S\,\sigma}{C_B\,(\,g/g_c\,)\,(\rho_L - \rho_v) + C_F\,(\,\tau_w/D_H\,)} \right]^{1/2} . \tag{36}$$

Assuming that the distance from the wall to the tip of the bubble is proportional to the bubble radius, a non-dimensional distance corresponding to this real distance can be given by

$$Y_B = \frac{(\sigma\,g_c\,D_H - \rho_L)^{1/2}}{\mu_L} \left[ 1 + C' \frac{g}{g_c} \frac{(\rho_L - \rho_v)\,D_H}{\tau_w} \right]^{-1/2} \tag{37}$$

where C and C' are appropriate constants. For those cases where the fluid forces are considerably greater than the buoyant forces this expression reduces to

$$Y_B = C\,(\sigma\,g_c\,D_H - \rho_L)^{1/2}\;\; 1/\mu_L \quad . \tag{38}$$

For the bubble to detach, the fluid temperature at the tip of the bubble must exceed the saturation temperature by an amount such that the pressure differential acting across the interface at the tip of the bubble balances the surface tension forces at the same position. By using the Clausius-Clapeyron solution of this pressure differential one finds that the fluid temperature-saturation temperature difference can be assumed to be zero.

The temperature at the tip of the bubble can also be specified from existing solutions for the fluid temperature distribution. Thus, if the flow is assumed to be turbulent, and using the solution proposed by Martinelli, we have

$$\begin{aligned} T_w - T_B &= \theta\,P_r\,Y_B \quad ; && 0 \le Y_B \le 5 \\ &= 5\theta\,\{Pr + \ln\,[1 + Pr\,(Y_B/5 - 1)]\} \quad ; && 5 \le Y_B \le 30 \\ &= 5\theta\,\{Pr + \ln\,[1 + 5\,Pr] + 0.5\,\ln\,[Y_B/30]\} \quad ; && Y_B \ge 30. \end{aligned} \tag{39}$$

The parameter $\theta$ is a non-dimensional term defined through the heat flux and liquid specific heat, that is,

$$\theta = \frac{q / A}{\rho_L \, C_{pL} \, (\tau_w g_c / \rho_L)^{1/2}} \quad . \tag{40}$$

Levy obtained values for the constants C and C' by correlation with available experimental data. Using the accepted heat-transfer relation from Dittus-Boelter, one obtains

$$hD_H/k_L = 0.023 \, (WD_H/\rho_L)^{0.8} \, (Pr)^{0.4} \quad . \tag{41}$$

Calculating the friction factor from

$$f = 0.0055\{1 + [20{,}000(e/D_H) + 10^6/(WD_H/\mu_L)]^{1/3}\}, \tag{42}$$

we are able to find the wall shear stress from

$$\tau_w = (f/8) \, (W^2/\rho_L \, g_c) \quad , \tag{43}$$

The correlation with experiment yielded values for the constants of

$$C = 0.015 \quad , \tag{44}$$

$$C' = 0 \quad .$$

Finally, from the definition of the heat transfer coefficient, one obtains

$$T_w - T = q''/h \quad , \tag{45}$$

and setting the bubble tip temperature, $T_B$, equal to the saturation temperature, $T_{sat}$, we can express the relationship between the saturation temperature, the wall temperature, and the fluid temperature at which the bubble would detach from the wall by

$$(T_w - T_{sat})/(T_w - T) = 0.023 \, (WD_H/\mu_L)^{-0.2} \, (Pr)^{-0.6} (f/8)^{-0.5} \, \Omega, \tag{46}$$

where $\Omega = Pr \, Y_B$ ; $\quad 0 \le Y_B \le 5$

$= 5 \{Pr + \ln [1 + Pr \, (0.2 \, Y_B - 1)]\}$ ; $\quad 5 \le Y_B \le 30$

$= 5 \{Pr + \ln (1 + 5Pr) + 0.5 \ln (Y_B/30)\}$ ; $\quad Y_B \ge 30.$

The solution of the force balance equation with void detachment was accomplished by iterating on the void detachment point to find where the right and left sides of Equation 46 were equal. The point at which the void was assumed to separate from the surface was taken as the point at which equality obtained.

The peak heat flux, that is, the heat flux at which there is a departure from nucleate boiling and the transition to film boiling begins, was determined by two correlations. The first, given by McAdams [32], indicates that the peak heat flux is a function of the fluid velocity and the fluid only. The second correlation is due to Bernath [33]. It encompasses a wider range of variables over which the correlation was made and it takes into account the effect of different flow geometries. It generally gives a lower value for the peak heat flux and is the value used here for determining the minimum DNB ratio, that is, the minimum ratio of the local allowable heat flux to the actual heat flux. In general, the McAdams correlation gives a DNB ratio 50% to 80% higher than the Bernath correlation.

Figure 4-22 shows the results of this analysis. Here we have plotted the maximum channel heat flux for which the DNB ratio is 1, with bulk pool water temperature as a parameter. It is assumed that all the vapor above the detachment point separates from the heated surface. From the figure it can be seen that with the design cooling water temperature at the core inlet (120°F) the maximum heat flux is 325 kBTU/hr-ft$^2$. For a 85 element core with an overall peak-to-average power density ratio of 2.0, this heat flux corresponds to a maximum reactor power of 1900 kW.

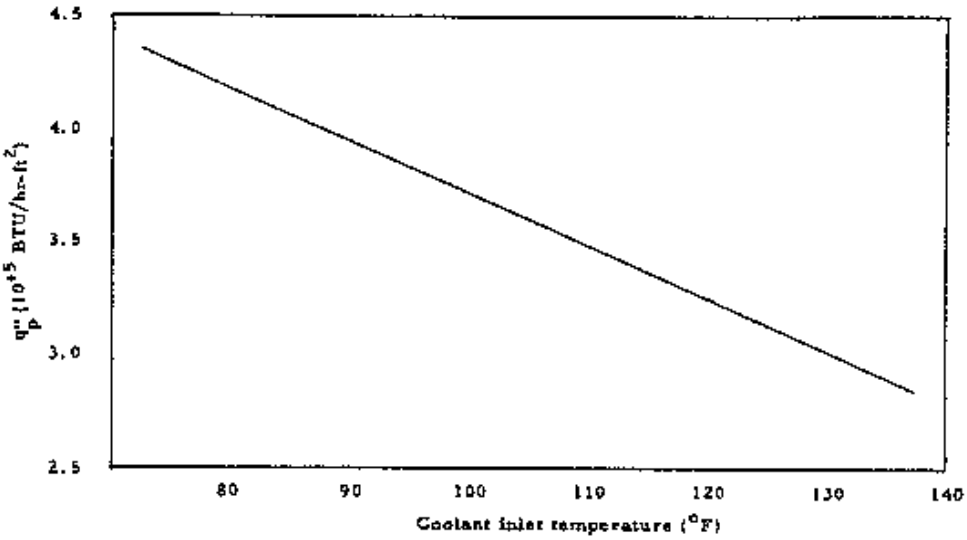


PLOT FOR WHICH DNB RATIO IS 1.0 OF
MAXIMUM HEAT FLUX VERSUS COOLANT TEMPERATURE

Figure 4-22

4.1.3.9. Nomenclature

| | |
|---|---|
| $A$ | cross-sectional area, $ft^2$ |
| $A_f$ | channel free flow area, $ft^2$ |
| $C$ | coolant specific heat, Btu/lb-°F |
| $d$ | diameter, in. |
| $D_e$ | channel equivalent diameter, ft |
| $D_H$ | hydraulic diameter, ft |
| $f_b$ | friction factor with subcooled boiling, dimensionless |
| $f_m$ | friction factor without boiling, dimensionless |
| $F$ | forces acting on vapor bubble |
| $g$ | constant, $4.18 \times 10^8$ $ft/hr^2$ |
| $h_b$ | heat transfer coefficient with subcooled boiling, Btu/hr-$ft^2$ -°F |
| $H$ | distance from midplane of heated channel to free surface of pool, ft |
| $K$ | pressure loss factor at channel inlet or exit, dimensionless |
| $n$ | number of equal axial increments into which heated length of core is subdivided |
| $N$ | Number of channels which receive their flow from a single opening in the lower grid plate |
| $p$ | absolute pressure, $lb/ft^2$ |
| $P$ | heated perimeter of channel, ft |
| $Pr$ | Prandtl number |
| $\delta p$ | pressure loss, $lb/ft^2$ |
| $q$ | heat load, Btu/hr |
| $q_t$ | total heat load to channel, Btu/hr |
| $q''$ | heat flux, Btu/hr-$ft^2$ |
| $q_p''$ | peak or "burnout" heat flux, Btu/hr-$ft^2$ |
| $r_B$ | bubble radius |
| $R_e$ | Reynolds number, dimensionless |
| $S/V$ | channel surface to volume ratio, $in.^{-1}$ |
| $T$ | coolant temperature, °F |
| $T_{sat}$ | coolant saturation temperature, °F |
| $v$ | specific volume, $ft^3/lb$ |
| $V$ | flow velocity, ft/hr |
| $W$ | mass flow rate, lb/hr |

| | |
|---|---|
| $Y$ | non-dimensional radius |
| $z$ | axial coordinate in channel, ft |
| $z_t$ | total length of channel, ft |
| $\delta z$ | length of a calculation increment in the channel, ft |
| $\mu$ | dynamic viscosity, ft-lb/hr |
| $\alpha$ | void fraction or fraction of a channel cross section which is occupied by vapor, dimensionless |
| $\sigma$ | surface tension, lb/ft |
| $\xi$ | vapor volume, or volume of vapor produced per unit area of heated surface, cubic in./square in. |
| $\nu$ | kinematic viscosity, $ft^2/hr$ |
| $\tau$ | shear stress, $lb/ft^2$ |
| $\rho$ | density, $lb/ft^3$ |
| $\epsilon/D_e$ | relative roughness |

Subscripts

| | |
|---|---|
| e | conditions at channel exit |
| i | conditions at channel entrance or inlet |
| l | conditions in portion of channel adjacent to lower reflector |
| m | conditions averaged over the liquid and vapor phases |
| o | bulk pool conditions |
| u | conditions in portions of channel adjacent to upper reflector |
| j | axial increment index |
| k | axial station index |
| w | conditions at cladding outer surface |
| v | vapor |
| L | liquid |

## 4.2. NUCLEAR DESIGN AND EVALUATION

The characteristics and operating parameters of this reactor have been calculated and extrapolated using experience and data obtained from existing TRIGA reactors as bench marks in evaluating the calculated data. There are several TRIGA systems with essentially the same core and reflector relationship as this TRIGA so the values presented here are felt to be accurate to within 5% but, of course, are influenced by specific core configuration details as well as operational details.

An operational core of 86 fuel elements, 3 fuel followed control rods, and one air followed control rod is to be arranged in 5 rings with a central, water filled hole. Dimension of the active fueled core, a cylinder, is 15 inches in height with an average radius of 8.6 inches. The cylinder radius is calculated as the average radius of a hexagonal fuel array with 91 unit cells (6 filled rings including the center hole) and a unit cell area of 2.55 square inches.

Table 4-3 summarizes the typical Mark II TRIGA reactor parameters for a core containing high-hydride, stainless steel clad fuel elements.

Table 4-3

TYPICAL TRIGA CORE NUCLEAR PARAMETERS

| | |
|---|---|
| Fuel elements | SS-clad U-$ZrH_{1.6}$ |
| Cold clean critical loading | ~64 elements |
| | ~2.5 kg U-235 |
| Operational loading | ~90 elements |
| | ~3.4 kg U-235 |
| $\ell$, Prompt neutron lifetime | 41 $\mu$sec |
| $\beta$, Effective delayed neutron fraction | 0.0070 |
| $\alpha$, Prompt negative temperature coefficient | $-1.0 \times 10^{-4}$ $\delta k/k°C$ |
| $T_f$ Average fuel temperature (1.1 MW) | 265°C |
| $T_w$ Average water temperature (1.1 MW) | 65°C |
| Water coolant volume to cell volume ratio | ~1/3 |

### 4.2.1. Reactivity Effects

The reactivity associated with the control rod is of interest both in the shutdown margin and in calculations of possible abnormal conditions related to reactivity accidents. Table 4-4 gives approximate reactivity values associated with a total control rod travel of 15 in. (38.1 cm), the full travel in the core.

Table 4-4

ESTIMATED CONTROL ROD NET WORTH

| Control Rod | diameter in. (cm) | $\delta k/k$ % |
|---|---|---|
| C ring - transient | 1.25 (3.18) | 2.1 |
| C ring - regulating | 1.35 (3.43) | 2.6 |
| D ring - shim 1 | 1.35 (3.43) | 2.0 |
| D ring - shim 2 | 1.35 (3.43) | 2.0 |

The maximum reactivity insertion rate is that associated with the transient rod which can be fully removed from the core in 0.1 sec producing an average reactivity insertion rate of 21% $\delta k/k$-sec.

The total reactivity worth of the control system is about 8.7%. With a core excess reactivity of 4.9%, the shutdown margin with all rods down is about 3.8% and with the most reactive rod stuck out is about 1%.

The reactivity worth of the fuel elements is dependent on their position within the core. Table 4-5 indicates the values that are expected in this installation.

Table 4-5

ESTIMATED FUEL ELEMENT REACTIVITY WORTH COMPARED WITH WATER AS A FUNCTION OF POSITION IN CORE

| Core Position | Worth (% $\delta k/k$) SS Clad U-$ZrH_{1.6}$ | Number of Fuel Positions |
|---|---|---|
| B ring | 1.07 | 6 |
| C ring | .85 | 12 |
| D ring | 0.54 | 18 |
| E ring | 0.36 | 24 |
| F ring | 0.25 | 30 |
| G ring | 0.19 | 36 |

Because of the prompt negative temperature coefficient a significant amount of reactivity is needed to overcome temperature and allow the reactor to operate at the higher power levels in steady-state operation. Figure 4-23 shows the relationship of reactor power level and associated reactivity loss to achieve a given power level. Figure 4-24 relates fuel temperature to a given steady-state reactor power level.

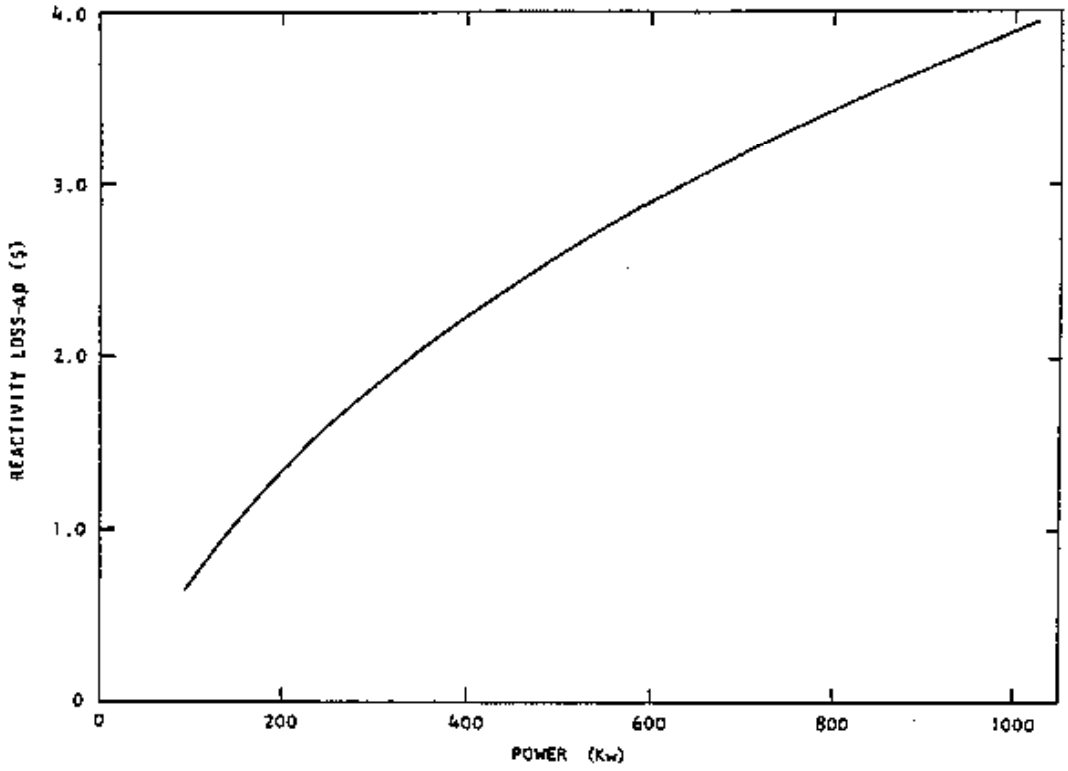


ESTIMATED REACTIVITY LOSS VERSUS POWER

Figure 4-23

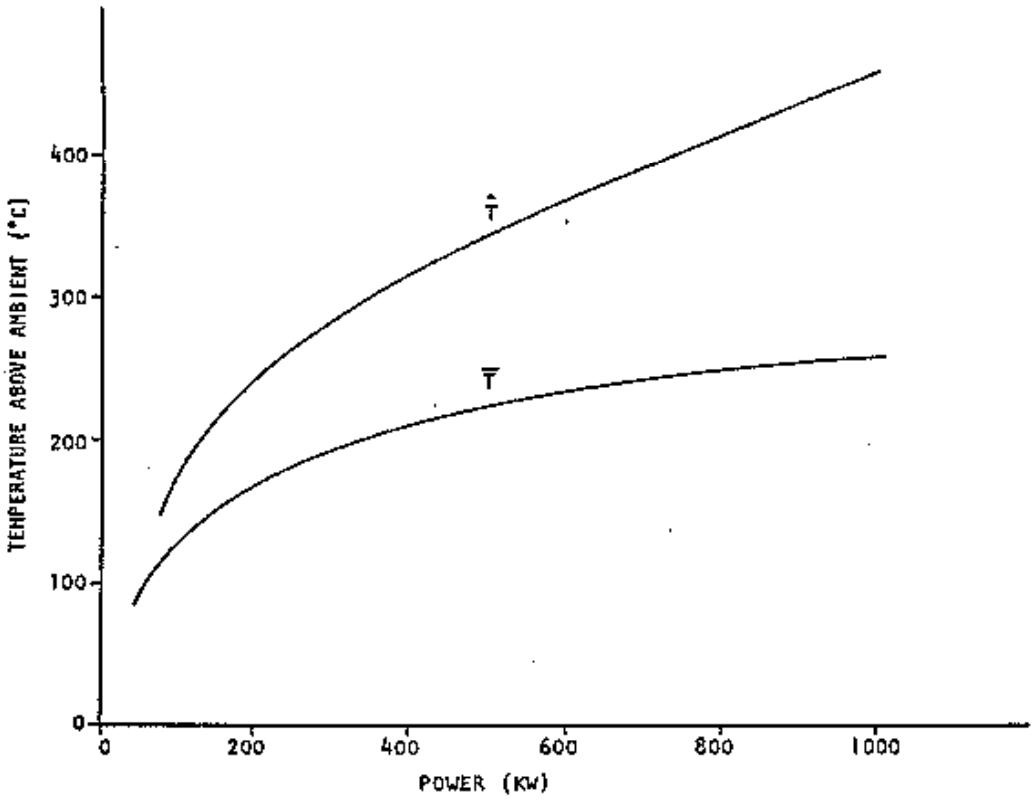


ESTIMATED MAXIMUM B RING AND
AVERAGE CORE TEMPERATURE VERSUS POWER

Figure 4-24

The reactivity effects associated with the insertion and removal of experiments in or around the core are difficult to predict; however, Table 4-6 is supplied to provide a guide to the magnitude of the reactivity effects associated with the introduction of experiments in the reactor core.

Table 4-6

EXPECTED REACTIVITY EFFECTS ASSOCIATED WITH EXPERIMENTAL FACILITIES

| | Worth (% δk/k) |
|---|---|
| Central thimble, fuel vs $H_2O$ | +0.90 |
| Central thimble, void vs $H_2O$ | -0.15 |
| Pneumatic transfer tube, (G ring) void vs $H_2O$ | -0.10 |
| Rotary specimen rack, void vs $H_2O$ | -0.20 |

4.2.2. Evaluation of Nuclear Design

The TRIGA reactor system is well-known for its conservative design. The stability of this reactor type has been proven both through calculations as well as through tests performed with the many TRIGA reactors in operation throughout the world. The stability of the TRIGA type reactor stems from the prompt negative temperature coefficient associated with the U-$ZrH_x$ fuel in conjunction with a suitable neutron thermalizing material. This TRIGA will have the stability that has been demonstrated on other TRIGA systems over the years.

A review of the reactivity worths associated with the reactor core indicates that no single item listed can produce a step reactivity insertion greater than that offered by routine pulse operation. In the pulsed mode of operation the results of a step insertion of $3.00 are far below those attributed to test pulses on the advanced TRIGA prototype reactor in which 3.5% δk/k was inserted in a step as is shown in Table 4-7.

A total reactivity limit for experiments is set at $3.00. This limit constrains the worst case transient accident to less than the design pulse insertion.

The possibility of a reactivity accident which could produce reactor powers and fuel temperatures attributed to a $4.00 step insertion has been considered and evaluated in the accident analysis section of this report. It is concluded from this analysis that the peak and average fuel temperatures resulting from this accident are well below the temperatures indicated as safety limits described in the reactor design bases of this document. It is further concluded that the integrity of the fuel containment will not be jeopardized and no adverse effects to the reactor system or personnel will arise from the advent of such an accident.

Table 4-7

COMPARISON OF REACTIVITY INSERTION EFFECTS

| | Pulse Resulting from Insertion of Maximum Excess Reactivity in This TRIGA | Max Pulse Tested on SS-Clad, High Hydride Fueled TRIGA types |
|---|---|---|
| Reactivity insertion, $ | 3.00 | 5.00 |
| Steady-State power before pulse, kW | < 1 | < 1 |
| Peak power, MW | ~1400 | ~8400 |
| Total energy release, MW-sec | ~18 | ~54 |
| Period, msec | ~3.1 | ~1.4 |
| Maximum fuel temperature, °C | ~540 | ~1050 |
| Pulse width, msec | ~11 | ~5.5 |

## 4.3 THERMAL AND HYDRAULIC DESIGN

This TRIGA reactor will be operated with natural convective cooling by reactor pool water. This method of heat dissipation is more than adequate for the power level of the reactor; i.e. 1100 kW(t). The thermal and hydraulic design of the reactor is well within the safety limits required to assure fuel integrity.

### 4.3.1. Design Bases

The thermal and hydraulic design for this TRIGA is based on assuring that fuel integrity is maintained during steady-state and pulsed mode operation as well as during those abnormal conditions which might be postulated for reactor operation. During steady-state operation fuel integrity is maintained by limiting reactor powers to values which assure that the fuel cladding can transfer heat from the fuel to the reactor coolant without reaching fuel-clad temperatures that could result in clad rupture. If these temperature conditions were exceeded, the maximum local heat flux in the core would be greater than the heat flux at which there is a departure from the nucleate boiling regime and consequently film blanketing of the fuel. This heat flux safety limit is a function of the inlet coolant temperature.

Figure 4-22 summarizes the results of the thermal and hydraulic analysis for steady-state operation of the TRIGA. In the figure critical heat flux for departure from nucleate boiling is plotted as a function of the coolant inlet temperature. The maximum power density in a TRIGA core is found by multiplying the average power density by a radial peak-to-average power generation ratio of 1.6 and an axial value of 1.25.

The correlation used to determine the heat flux at which there is a departure from nucleate boiling is from Bernath [33]. This correlation encompasses a wider range of experimental data than the usual correlations, e.g., the correlation due to McAdams, and, generally gives a lower value for the DNB ratio than the other correlations.

Table 4-8

1000 kW(t) TRIGA HEAT TRANSFER AND HYDRAULIC PARAMETERS

| | |
|---|---|
| Number of fuel elements | 90 |
| Diameter | 1.475 in. |
| Length (heated) | 15.0 in. |
| Flow area | 0.522 $ft^2$ |
| Wetted perimeter | 34.75 ft |
| Hydraulic diameter | 0.0601 ft |
| Heat transfer surface | 43.44 $ft^2$ |
| Inlet coolant temperature | 120°F (48.9°C) |
| Exit coolant temperature (average) | 174°F (78.9°C) |
| Coolant mass flow | 63,700 lb/hr |
| Average flow velocity | 0.55 ft/sec |
| Average fuel temperature | 500°F (260°C) |
| Maximum wall temperature | 280°F (138°C) |
| Maximum fuel temperature | 842°F (450°C) |
| Average heat flux | 78,600 Btu/hr-$ft^2$ |
| Maximum heat flux | 157,100 Btu/hr-$ft^2$ |
| Minimum DNB ratio | 2.0 |

Table 4-8 lists the pertinent heat transfer and hydraulic parameters for the TRIGA operating at a nominal power level of 1000 kW. These data were taken from the results of calculations described in Section 4.1.

During pulsing operation the limiting thermal-hydraulic condition is the fuel temperature and the corresponding $H_2$ excess pressure beyond which clad rupture may occur. As indicated in Section 4.1, coolant temperature is not a limiting condition in pulsing since heating conditions are essentially adiabatic and significant transfer of heat energy to the coolant does not occur until after peak fuel-clad temperatures occur.

The safety limit on fuel temperature occurring in the pulse mode of operation is 1150°C. This temperature will give an internal equilibrium hydrogen pressure (U-ZrH fuel H/Zr; 1.6) less than that which would produce a stress equivalent to the ultimate strength of the clad at a temperature of 680°C. This clad temperature is higher than would actually occur and therefore conservative even in the case of a pulse producing a peak adiabatic fuel temperature of 1150°C.

### 4.3.2. Thermal and Hydraulic Design Evaluation

The validity and safety of the TRIGA thermal-hydraulic design is established in Section 4.1. In that section it is shown that design-basis conditions evaluated for TRIGA reactors using stainless steel clad U-ZrH (H/Zr; 1.6) fuel elements provide a generous safety margin for this TRIGA. These general evaluations are supported by extensive experience in operation of TRIGA cores at equivalent fuel temperatures and reactor power levels. No adverse results are reported from other similar TRIGA reactors with comparable fuel temperatures and power levels.

## 4.4. MECHANICAL DESIGN AND EVALUATION

### 4.4.1. General Description

The TRIGA Mark II reactor core assembly is located near the bottom of an elongated cylindrical aluminum tank surrounded by a reinforced concrete structure. A typical installation is shown in Figure 4-25. The standard reactor tank is a welded aluminum vessel with 1/4 in. thick (0.64 cm.) walls, a diameter of approximately 6.5 feet (2 meters), and a depth of at least 25 feet (7.6 m.). The tank is all-welded for water tightness. The integrity of the weld joints is verified by radiographic testing, dye penetrant checking, and helium leak testing. The outside of the tank is coated for corrosion protection.

An aluminum angle used for mounting the ion chambers, fuel storage racks, underwater lights, and other equipment, is located around the top of the tank. Demineralized water in the tank is provided such that at least 21 feet (6.4 m.) of shielding water is above the core. The core is shielded radially by a minimum of 7.97 feet (2.43 m) of concrete with a density of 2.88 gm/cc, 1.5 feet (~45 cm.) of water, and 10.2 inches (25.9 cm.) of graphite reflector (see Figure 4-26).

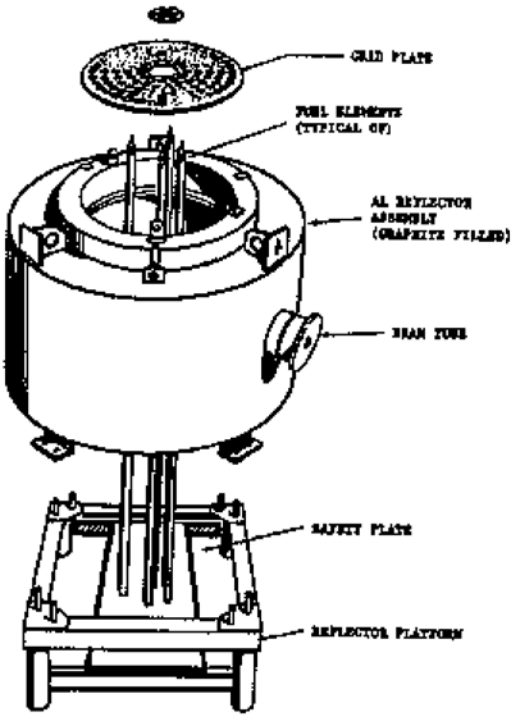


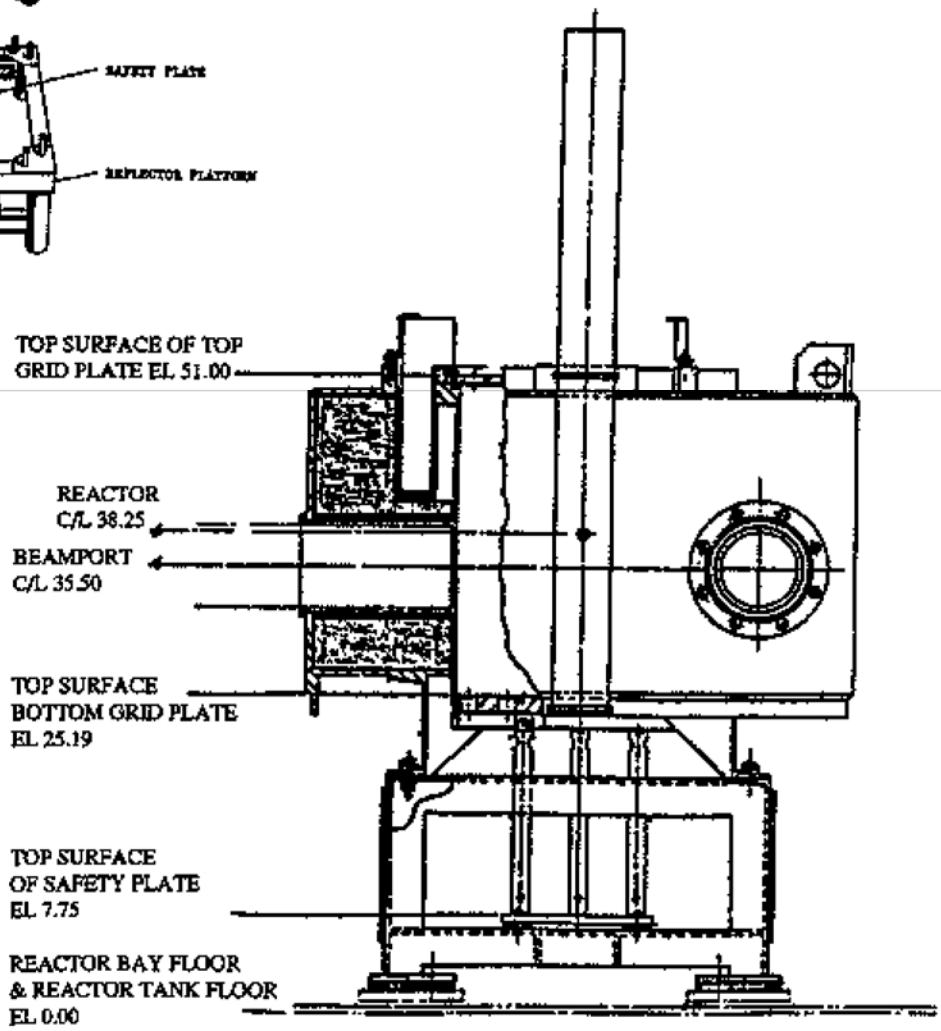


TRIGA reactor - elevation view

REACTOR, REFLECTOR, AND SHIELDING

Figure 4-25

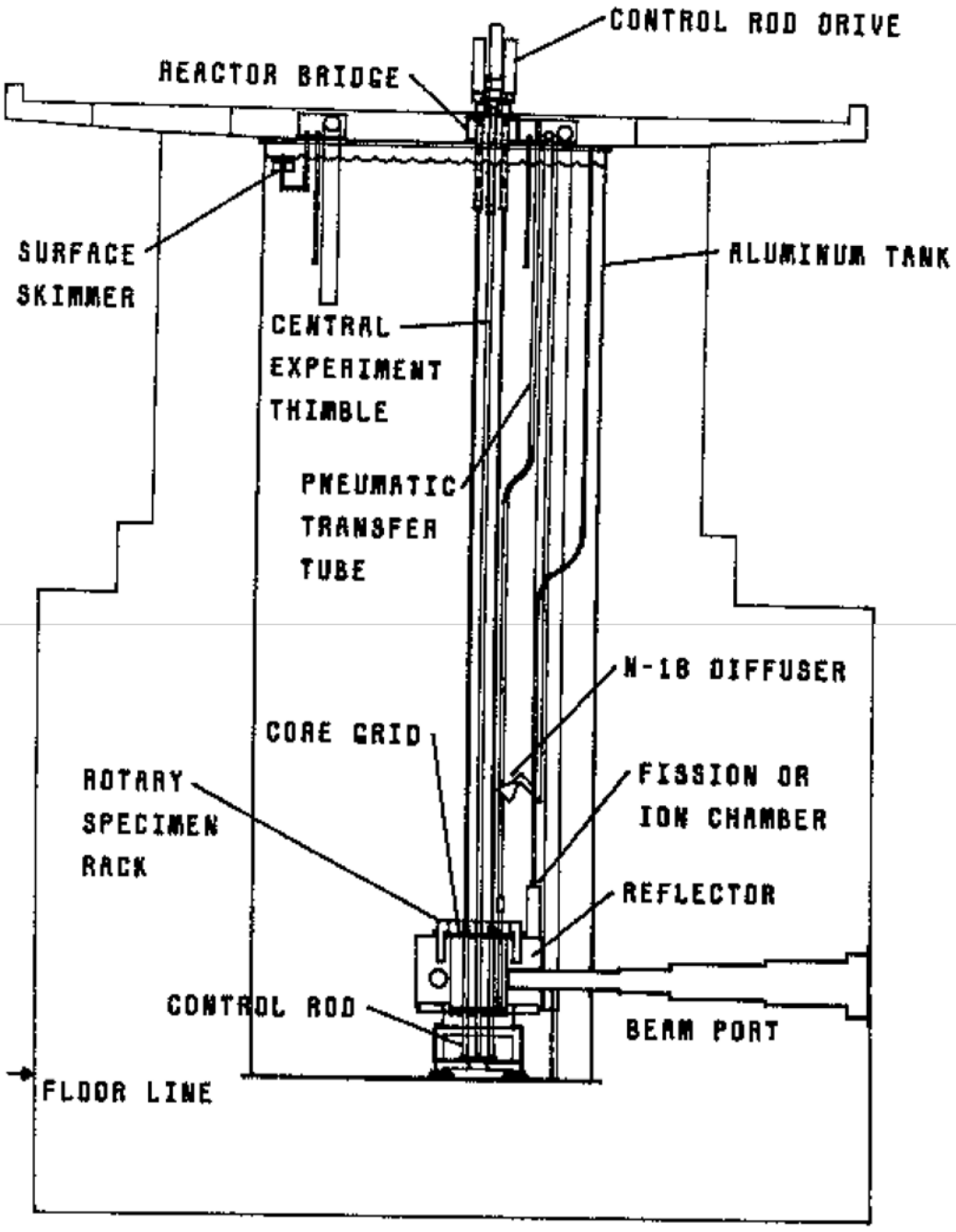


TRIGA MARK II REACTOR

Figure 4-26

### 4.4.2. Reflector Assembly

The reflector is a ring-shaped block of graphite that surrounds the core radially. The graphite is 10.2 inches (25.91 cm.) thick radially, with an inside diameter of 21-5/8 inches (54.93 cm.) and a height of 21-13/16 inches (54.40 cm.) The graphite is protected from water penetration by a leak-tight welded aluminum can.

A "well" in the top of the graphite reflector is provided for the rotary specimen rack. This well is also aluminum-lined, the lining being an integral part of the aluminum reflector can. The rotary specimen rack is a self-contained unit and does not penetrate the sealed reflector at any point.

The graphite, and outer surface of the aluminum can are pierced by an aluminum tube which forms the inner section of beam ports that penetrate the reflector. The reflector penetrating beam tubes are connected by aluminum couplings to the corresponding beam tube section fabricated as part of the reactor tank structure.

The reflector assembly rests on an aluminum platform at the bottom of the tank, and provides support for the two grid plates and the safety plate. Three lugs are provided for lifting the assembly.

### 4.4.3. Grid Plates

The top grid plate is an aluminum plate 5/8 inches (1.59 cm.) thick (3/8 inches, 0.95 cm., thick in the central region) that provides accurate lateral positioning for the core components. The plate is supported by a ring welded to the top inside surface of the reflector container and is anodized to resist wear and corrosion.

One hundred twenty one (121) holes, 1.505 inches (3.823 cm.) diameter, are drilled into the top grid plate in a modified hexagonal pattern (the vertexes of the hex are omitted) around a central hole. The holes are to locate the fuel-moderator and graphite dummy elements, the control rods and guide tubes, and the pneumatic transfer tube. (See Figure 4-27.) An equivalent diameter center hole accommodates the central thimble. Small holes at various positions in the top grid plate permit insertion of wires or foils into the core to obtain flux data.

A hexagonal section can be removed from the center of the upper grid plate for the insertion of specimens up to 4.4 inches (11.18 cm.) in diameter into the region of highest flux; this requires prior relocation of the six fuel elements from the B ring to the outer portion of the core and removal of the central thimble. This removable section will not be used initially; a license amendment will be obtained prior to its use.

Two generally triangular-shaped sections are cut out of the upper grid plate. Each cut out encompasses two E and one D ring holes. Fuel elements placed in these locations, require lateral support by a special fixture. When the fuel elements and support are removed, there is room for inserting specimens up to 2.4 inches (6.1 cm.) in diameter.

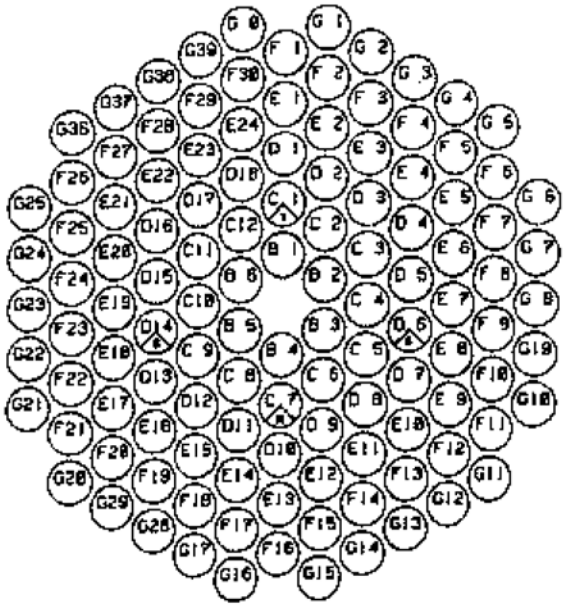

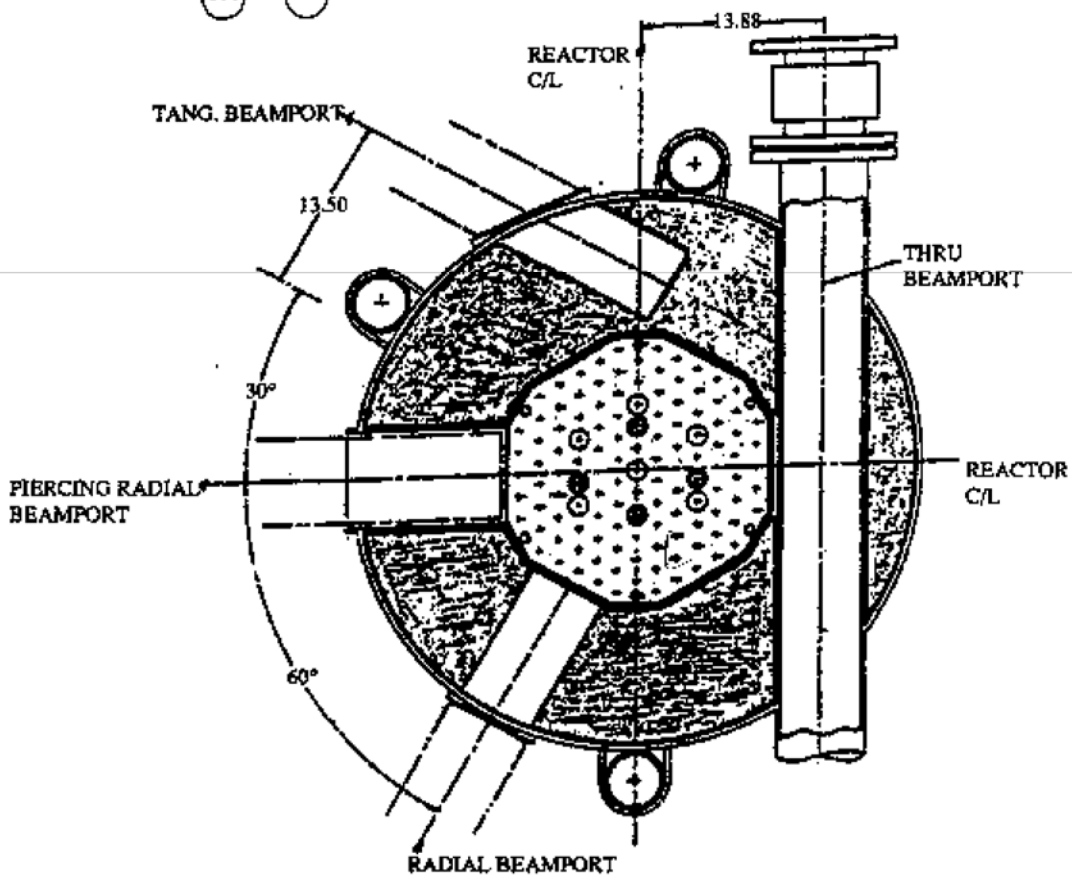


TRIGA reactor - cross section through beamports

CORE ARRANGEMENT

Figure 4-27

The bottom grid plate is an aluminum plate 3/4 inch (1.91 cm.) thick which supports the entire weight of the core and provides accurate spacing between the fuel-moderator elements. Six pads around a hexagonal ring which is welded to the reflector container support the bottom grid plate.

Holes in the bottom grid plate are aligned with fuel element holes in the top grid plate. They are countersunk to align the adaptor end of the fuel-moderator elements and the adaptor end of other in core experiment systems, such as the pneumatic transfer tube.

The differential area between the fitting at the top of the fuel elements and the round holes in the top grid plate permits passage of cooling water through the plate.

### 4.4.4. Safety Plate

The safety plate is provided to preclude the possibility of control rods falling out of the core. It is a 1/2 inch (1.27 cm.) thick plate of aluminum set on the core support structure below the reflector. The plate is placed about 16 inches (40.6 cm.) below the bottom grid plate.

A central hole of 1.505 inches (3.823 cm.) in diameter in the lower grid serves as a clearance hole for the central thimble. Eight additional 1.505-inch (3.823 cm.) diameter holes are aligned with upper grid plate holes to provide passage of fuel-follower control rods. Those holes in the bottom grid plate not occupied by control rod followers are plugged with removable fuel element adaptors that rest on the safety plate. These fuel element adaptors are solid aluminum cylinders 1.5 inches (3.81 cm.) in diameter by 17 inches (43.18 cm.) long. At the lower end is a fitting that is accommodated by a hole in the safety plate. The upper end of the cylinder is flush with the upper surface of the bottom grid plate when the adaptor is in place. This end of the adaptor has a hole similar to that in the bottom grid plate for accepting the fuel element lower end fitting. With the adaptor in place, a position formerly occupied by a control rod with a fuel follower will now accept a standard fuel element. The adaptor can be removed with a special handling tool.

### 4.4.5. Fuel-Moderator Elements

The active part of each fuel-moderator element, shown in Figure 4-28, is approximately 1.43 in. (3.63 cm.) in diameter and 15 in. long (38.1 cm.). The fuel is a solid, homogeneous mixture of uranium-zirconium hydride alloy containing about 8.5% by weight of uranium enriched to 20% U-235. The hydrogen-to-zirconium atom ratio is about 1.6. To facilitate hydriding, a small hole is drilled through the center of the active fuel section and a zirconium rod is inserted in this hole after hydriding is complete. The hydriding hole and zirconium rod are not shown in Figure 4-28. Several types of end fittings exist, therefore, those shown are typical.

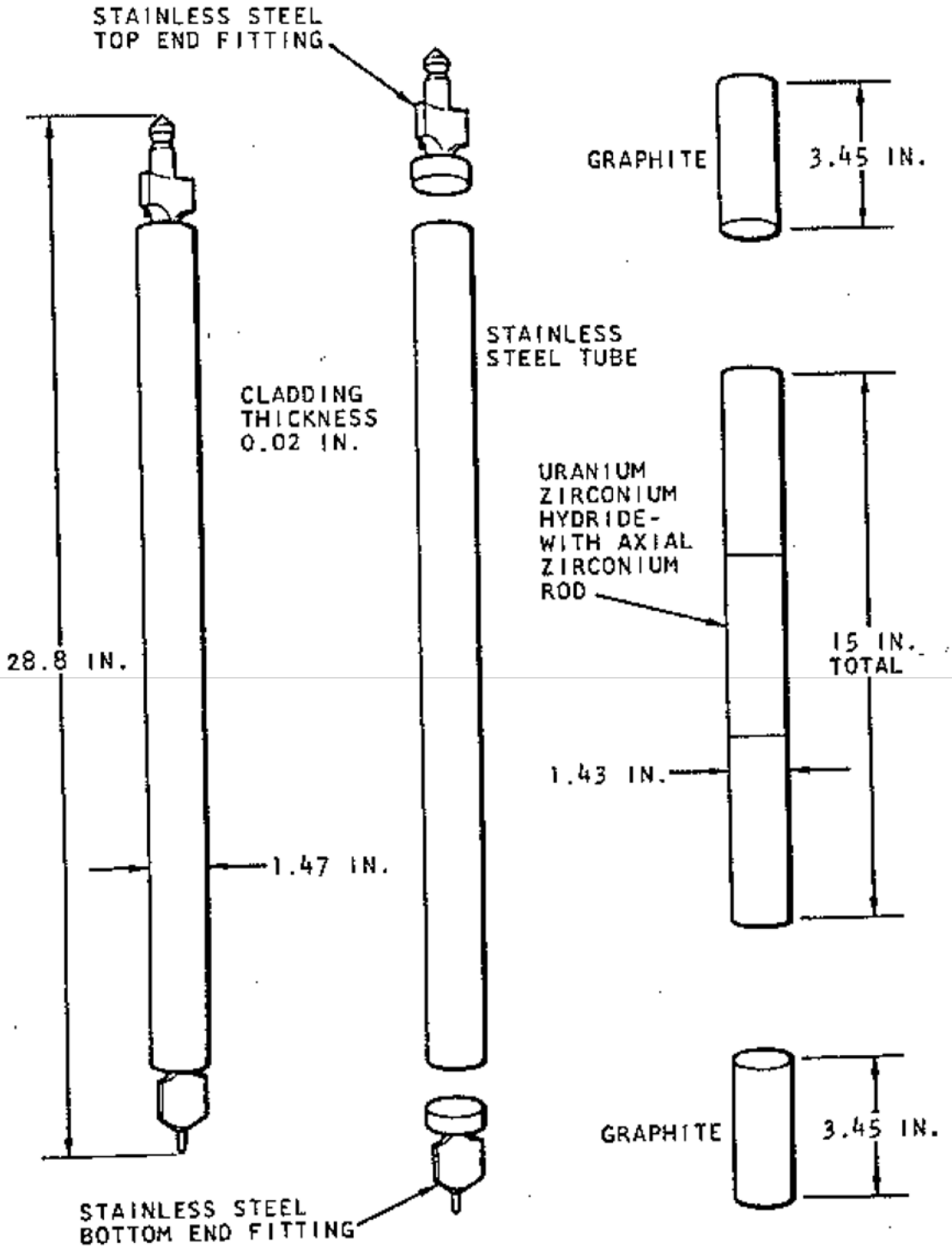


TRIGA STAINLESS STEEL CLAD
FUEL ELEMENT WITH END FITTINGS

Figure 4-28

Each element is clad with a 0.020 in. thick (.508 mm.) stainless steel can, and all closures are made by heliarc welding. Two sections of graphite are inserted in the can, one above and one below the fuel, to serve as top and bottom reflectors for the core. Stainless steel end fixtures are attached to both ends of the can, making the overall length of the fuel-moderator element 28.8 in. (73.2 cm.).

The lower end fixture supports the fuel-moderator element on the bottom grid plate. The upper end fixture consists of a knob for attachment of the fuel-handling tool and a triangular spacer, which permits cooling water to flow through the upper grid plate. The total weight of a fully-loaded fuel element is about 3.18 kg. (7 lb.).

4.4.5.1 Instrument Fuel Elements

An instrumented fuel-moderator element will have three thermocouples embedded in the fuel. As shown in Figure 4-29, the sensing tips of the fuel element thermocouples are located about 0.3 in. (0.76 cm.) from the vertical centerline. Thermocouple specifications are listed in Table 4-9.

The thermocouple lead wires pass through a seal in the upper end fixture. A lead tube provides a watertight conduit carrying the lead wires above the water surface in the reactor pool. Thermocouple specifications are listed in Table 4-9. In other respects the instrumented fuel-moderator element is identical to the standard element.

Table 4-9

THERMOCOUPLE SPECIFICATIONS

| | |
|---|---|
| Type | Chromel-alumel |
| Wire diameter | 0.005 in. |
| Resistance | 24.08 ohms/double foot at 68°F |
| Junction | Grounded |
| Sheath material | Stainless steel |
| Sheath diameter | 0.040 in. |
| Insulation | MgO |
| Lead-out wire | |
| Material | Chromel-alumel |
| Size | 20 AWG |
| Color code | Chromel - yellow (positive)<br>Alumel - red (negative) |
| Resistance | 0.59 ohms/double foot at 75°F |

4.4.5.2. Evaluation of Fuel Element Design.

General Atomic has acquired extensive experience in the fabrication and operation of high hydride, stainless steel clad fuel elements. As shown in other sections of this report, the stresses associated with the fuel and cladding temperatures in all modes of operation, normal and abnormal, are within the safety limits described in the Reactor Design Bases.

Dimensional stability of the overall fuel element has been excellent in the TRIGA reactors in operation. Analysis of the heat removal from elements that touch owing to transverse bending shows that the contact will not result in hot spots that damage the fuel.

Tests have been conducted on TRIGA fuel elements to determine the strength of the fuel element clad when subjected to internal pressure. At room temperature the clads ruptured at about 2050 psig. This corresponds to a hoop stress at rupture of about 72,000 psi which compares favorably with the minimum expected value for 304 stainless steel.

It is concluded that the chemical stability of U-$ZrH_{1.6}$ fuel-moderator material does not impose a safety limit on reactor operation (see Section 4.1.1). Table 4-10 gives a summary of the fuel element specifications.

Table 4-10

SUMMARY OF FUEL ELEMENT SPECIFICATIONS

| | Nominal Value | |
|---|---|---|
| Fuel-Moderator Material | | |
| H/Zr ratio | 1.6 | |
| Uranium content | 8.5 wt % | |
| Enrichment (U-235) | 19.7 #0.2 | |
| Diameter | 1.43 in. | |
| Length | 15 in. | |
| Graphite End Reflectors | Upper | Lower |
| Porosity | 20% | 20% |
| Diameter | 1.43 in. | 1.43 in. |
| Length | 3.44 in. | 3.47 in. |
| Cladding | | |
| Material | Type 304 SS | |
| Wall thickness | 0.020 in. | |
| Length | 22.10 in. | |
| End Fixtures and Spacer | Type 304 SS | |
| Overall Element | | |
| Outside diameter | 1.47 in. | (3.73 cm) |
| Length | 28.37 in. | (72.06 cm) |
| Weight | 7 lb. | (3.18 kg) |

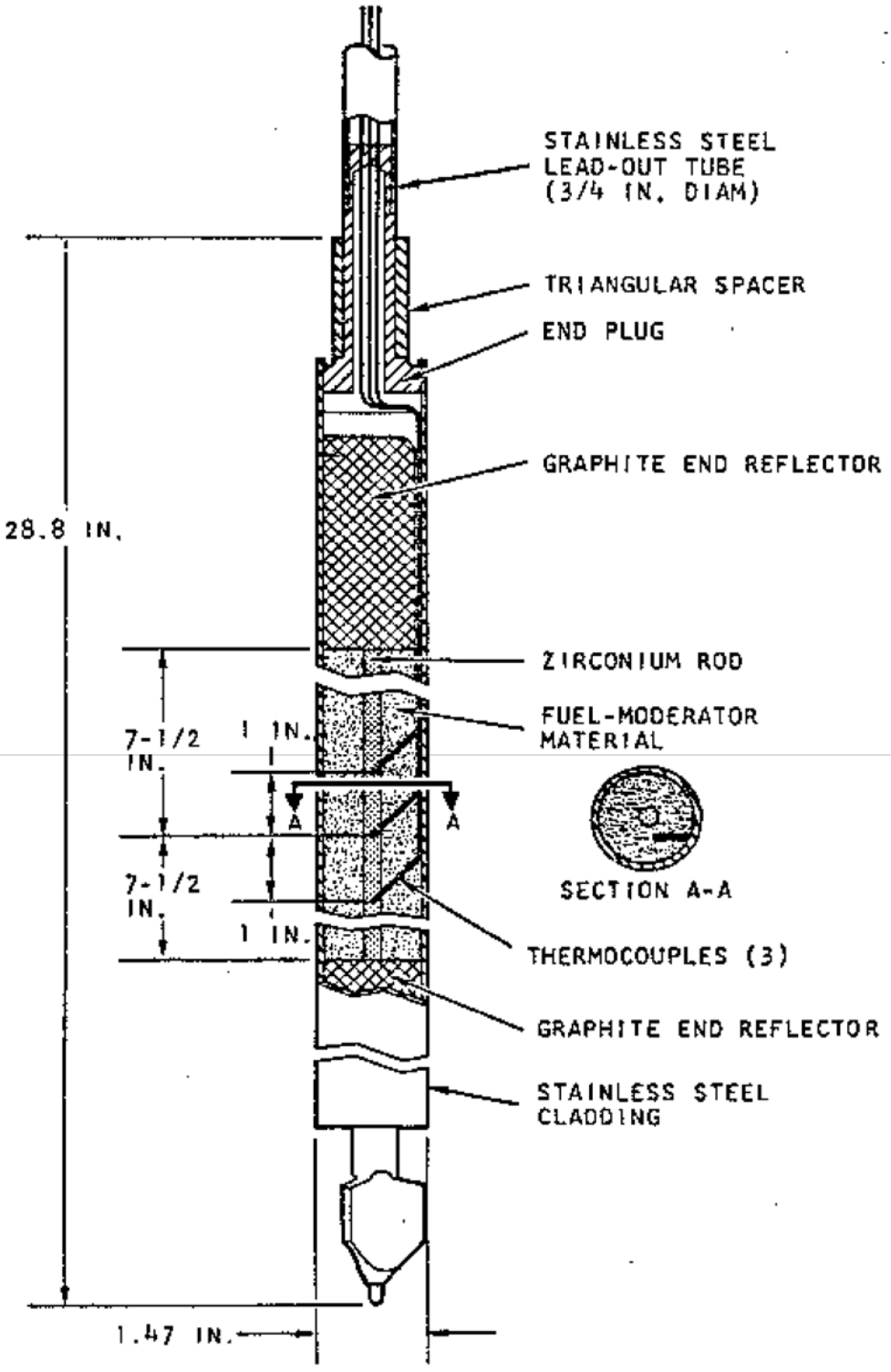


INSTRUMENTED FUEL ELEMENT

Figure 4-29

Most of the fuel for the initial core loading will consist of elements with burnups of a fraction of a MW-day to several MW-days. It is anticipated that an initial core loading of about 94 fuel elements, including instrumented elements, and fuel followed control rods, will produce a cold, clean excess reactivity of -4.9% $\delta k/k$. The operational core configuration will contain two instrumented fuel elements with at least one located in the inner most reactor ring.

### 4.4.6. Neutron Source and Holder

A 2 or 3 curie americium beryllium neutron source will be used for startup. The neutron source holder is made of aluminum, is cylindrical in shape, and has a cavity to hold the source. The source holder can be installed in a vacant fuel or graphite element location. A shoulder at the upper end of the holder supports the assembly on the upper grid plate, the rod itself, which contains the source, extending down into the core region. The neutron source is contained in a cavity in the lower portion of the rod assembly at the horizontal centerline of the core. This cylindrical cavity is 0.981 in. (2.492 cm.) in diameter and approximately 3 in. (7.62 cm.) deep. The upper and lower portions are screwed together. A soft aluminum ring provides sealing against water leakage into the cavity. Since the upper end fixture of the source holder is similar to that of the fuel element, the source holder can be installed or removed with the fuel handling tool. In addition, the upper end fixture has a small hole through which one end of a stainless steel wire may be inserted to facilitate handling operation from the top of the tank.

### 4.4.7. Graphite Dummy Elements

Graphite dummy elements may be used to fill grid positions not filled by the fuel-moderator elements or other core compounds. They are of the same general dimensions and construction as the fuel-moderator elements, but are filled entirely with graphite and are clad with aluminum.

### 4.4.8. Control System Design

The reactor uses four control rods:

a. Shim rod 1

b. Shim rod 2

c. A transient rod

d. A regulatory rod

The regulating and shim rods are sealed 304 stainless steel tubes approximately 43 in. (109 cm) long by 1.35 in. (3.43 cm) in diameter in which the uppermost 6.5 in. (16.5 cm) section is an air void and the next 15 in. (38.1 cm) is the neutron absorber (boron carbide in solid form). Immediately below the neutron absorber is a fuel follower section consisting of 15 in. (38.1 cm) of U-$ZrH_{1.6}$ fuel. The bottom section of the rod is 6.5 in. (16.5 cm) air void.

The regulating and shim rods pass through and are guided by 1.5 in. (3.81 cm) diameter holes in the top and bottom grid plates. A typical control rod with fuel follower is shown in the withdrawn and inserted positions in Figure 4-30.

The safety-transient rod is a sealed, 36.75 in. (93.35 cm) long by 1.25 in. (3.18 cm) diameter tube containing solid boron carbide as a neutron absorber. Below the absorber is an air filled follower section. The absorber section is 15 in. (38.1 cm) long and the follower is 20.88 in. (53.02 cm) long. The transient rod passes through the core in a perforated aluminum guide tube. The tube receives its support from the safety plate and its lateral positioning from both grid plates. It extends approximately 10 in. (25.4 cm) above the top grid plate. Water passage through the tube is provided by a large number of holes distributed evenly over its length. A locking device is built into the lower end of the assembly.

The control rods are connected to their individual drive units by screwing the upper end of the rod into a control rod drive assembly connecting rod. Vertical travel of each rod is approximately 15 in. (38.1 cm). Reactivity worths and core positions for each rod are summarized in the section on nuclear design. A summary of other control rod design parameters is given in Table 4-11.

Table 4-11

SUMMARY OF CONTROL ROD DESIGN PARAMETERS

| | Transient | Shim and Regulating |
|---|---|---|
| <u>Cladding</u> | | |
| Material | Al | Type 304 SS |
| OD | 1.25 in. (3.18 cm) | 1.35 in. (3.43 cm) |
| Length | 36.75 in. (93.35 cm) | 43.13 in. (109.5 cm) |
| Wall thickness | 0.028 in. (0.071 cm) | 0.020 in. (0.051 cm) |
| <u>Absorber</u> | | |
| Material | Boron Carbide (solid form) | |
| OD | 1.19 in. (3.02 cm) | 1.31 in. (3.32 cm) |
| Length | 15 in. (38.1 cm) | 14.25 in. (36.20 cm) |
| <u>Follower</u> | | |
| Material | Air | $U\text{-}ZrH_{1.6}$ |
| OD | 1.25 in. (3.18 cm) | 1.31 in. (3.34 cm) |
| Length | 20.88 in. (53.02 cm) | 15 in. (38.1 cm) |

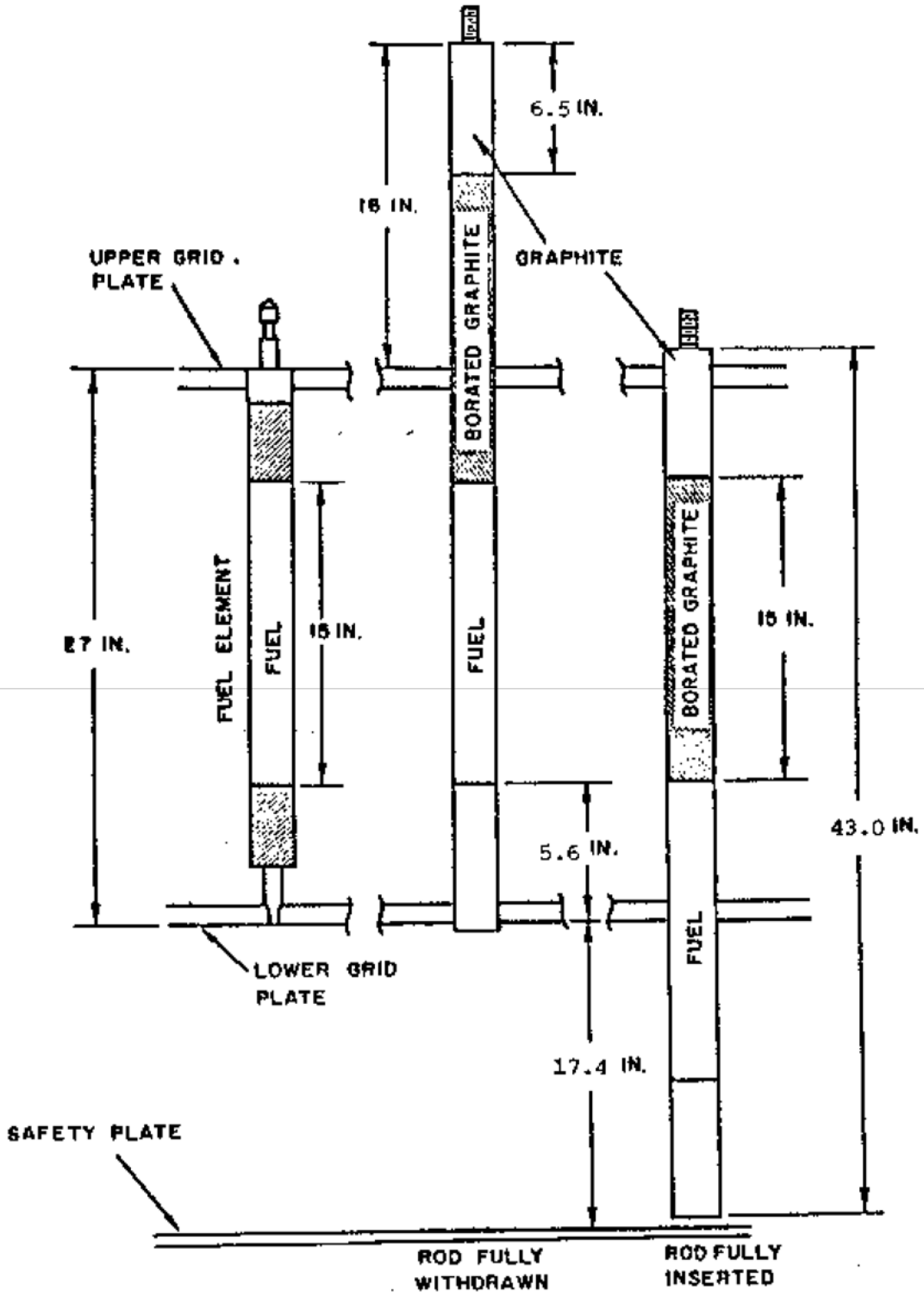


FUEL FOLLOWED CONTROL ROD

Figure 4-30

4.4.8.1. Control Rod Drive Assemblies.

The control rod drive assemblies for the shim rods are mounted on a bridge assembly over the pool and consist of a motor and reduction gear driving a rack-and-pinion as indicated in Figure 4-31. A helipot connected to the pinion generates the position indication. Each control rod drive has a tube that extends to a dashpot below the surface of the water. The control rod assembly is connected to the rack through an electromagnet and armature. In the event of a power failure or scram signals, the control rod magnets are de-energized and the rods fall into the core. The time required for a rod to drop into the core from the full-out position is about 1 second.

The rod drive motor is non-synchronous, single-phase, and instantly reversible, and will insert or withdraw the control rod at a rate of approximately 18 in./min. (0.75 cm/sec) for the shim 1 and shim 2 rods. The regulating rod design is similar to the shim rods except for the type of rod drive.

A key-locked switch on the control console power supply prevents unauthorized operation of all control rod drives. Electrical dynamic and static braking on the motors are used for fast stops.

Limit switches mounted on the drive assembly actuate circuits which indicate the following:

a. The "up" and "down" positions of the magnet

b. The "down" position of the rod

c. The magnet in contact with the rod

4.4.8.2. Regulating Rod and Stepping Motor Drive

The rod drive mechanism for the regulating rod will be an electric stepping-motor-actuated linear drive equipped with a magnetic coupler and a positive feedback potentiometer.

A stepping motor drives a pinion gear and a 10-turn potentiometer via a chain and pulley gear mechanism. The potentiometer is used to provide rod position information. The pinion gear engages a rack attached to the magnet draw tube. An electromagnet, attached to the lower end of the draw tube, engages an iron armature. The armature is screwed and pinned into the upper end of a connecting rod that terminates at its lower end in the control rod. When the stepping motor is energized (via the rod control UP/DOWN switch on the operator's console), the pinion gear shaft rotates, thus raising the magnet draw tube, the armature and the connecting rod will raise with the draw tube so that the control rod is withdrawn from the reactor core. In the event of a reactor scram, the magnet is de-energized and the armature will be released. The connecting rod, the piston, and the control rod will then drop, thus reinserting the control rod.

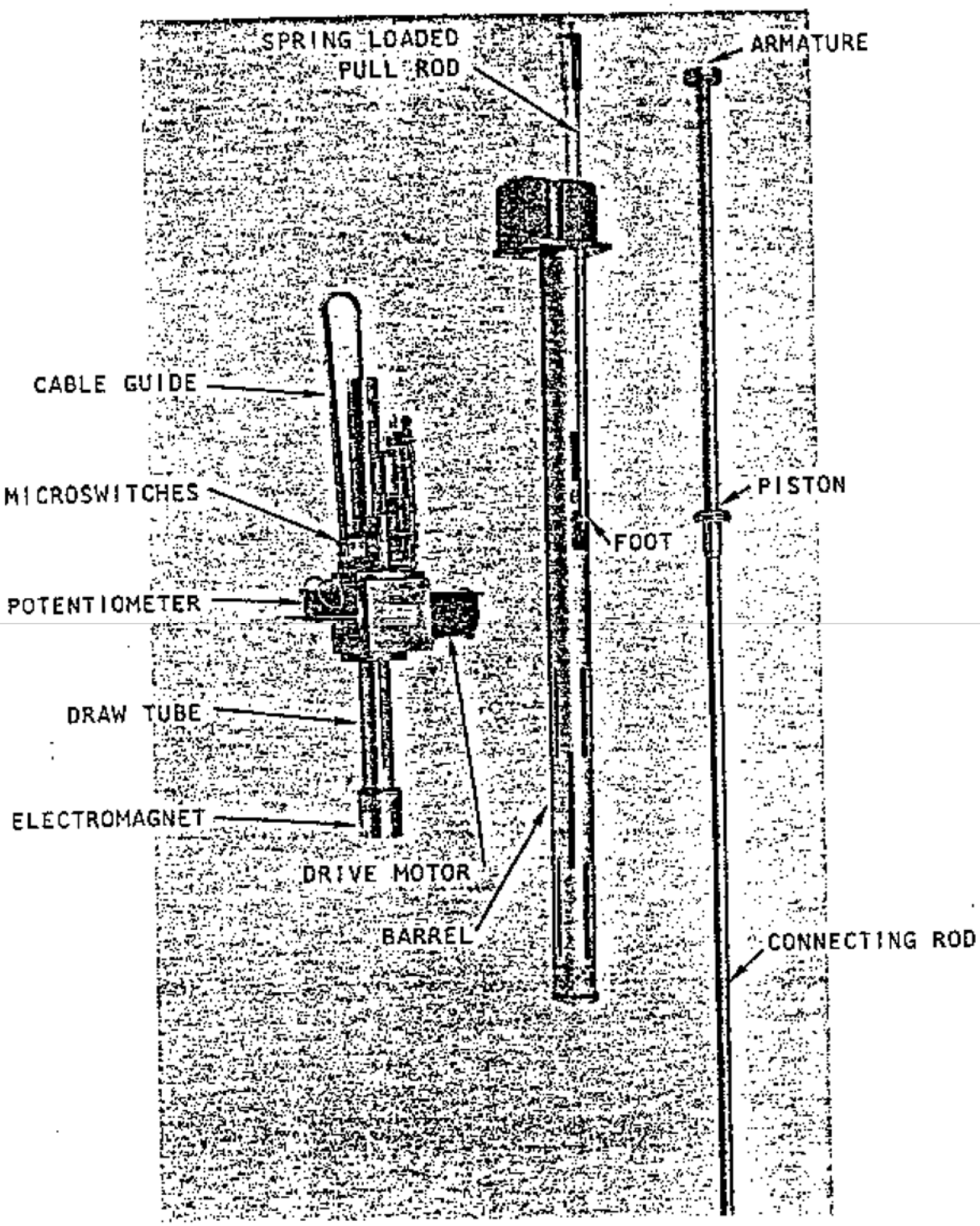


RACK AND PINION CONTROL ROD DRIVE

Figure 4-31

Stepping motors operate on phase-switched direct current power. The motor shaft advances 200 steps per revolution (1.8 degrees per step). Since current is maintained on the motor windings when the motor is not being stepped, a high holding torque is maintained.

The torque vs speed characteristic of a stepping motor is greatly dependent on the drive circuit used to step the motor. To optimize the torque characteristic vs motor frame size, a Translator Module was selected to drive the stepping motor. This combination of stepping motor and translator module produces the optimum torque at the operating speeds of the control rod drives. Characteristic data for the drive indicate a possible travel rate of 33 ipm (1.40 cm/s). Measurements of the actual rate provide a speed of 27 ipm (1.14 cm/s).

4.4.8.3. Transient Rod Drive Assembly.

The safety transient control rod on pulsing TRIGA Mark II reactors is operated with a pneumatic rod drive (see Figures 4-32 and 4-33). Operation of the transient rod drive is controlled from the reactor console.

The transient rod is a scrammable rod operated in both pulse and stead-state modes of reactor operation. During non pulse operation, the transient rod will function as an alternate safety rod with air continuously supplied to the rod. Rod position is thus controlled by operation of an electric motor that positions the air drive cylinder. The position of the transient control rod and its associated reactivity worth will generally dictate removal of the rod as the first step of a startup for steady-state operation. Rod withdrawal speed is about 28ipm (1.19cm/s).

The transient rod drive is mounted on a steel frame that bolts to the bridge. Any value from zero to a maximum of 15 in. (38.1 cm.) of rod may be withdrawn from the core; administrative control is exercised to restrict its travel so as not to exceed the maximum licensed step insertion of reactivity ($3.14 or 2.2% $\delta k/k$).

The transient rod drive is a single-acting pneumatic cylinder with its piston attached to the transient rod through a connecting rod assembly. The piston rod passes through an air seal at the lower end of the cylinder. Compressed air is supplied to the lower end of the cylinder from an accumulator tank when a three-way solenoid valve located in the piping between the accumulator and cylinder is energized. The compressed air drives the piston upward in the cylinder and causes the rapid withdrawal of the transient rod from the core. As the piston rises, the air trapped above it is pushed out through vents at the upper end of the cylinder. At the end of its travel, the piston strikes the anvil of an oil-filled hydraulic shock absorber, which has a spring return, and which decelerates the piston at a controlled rate over its last 2 in. (5 cm.) of travel. When the solenoid is de-energized, the valve cuts off the compressed air supply and exhausts the pressure in the cylinder, thus allowing the piston to drop by gravity to its original position and restore the transient rod to its fully inserted position in the reactor core.

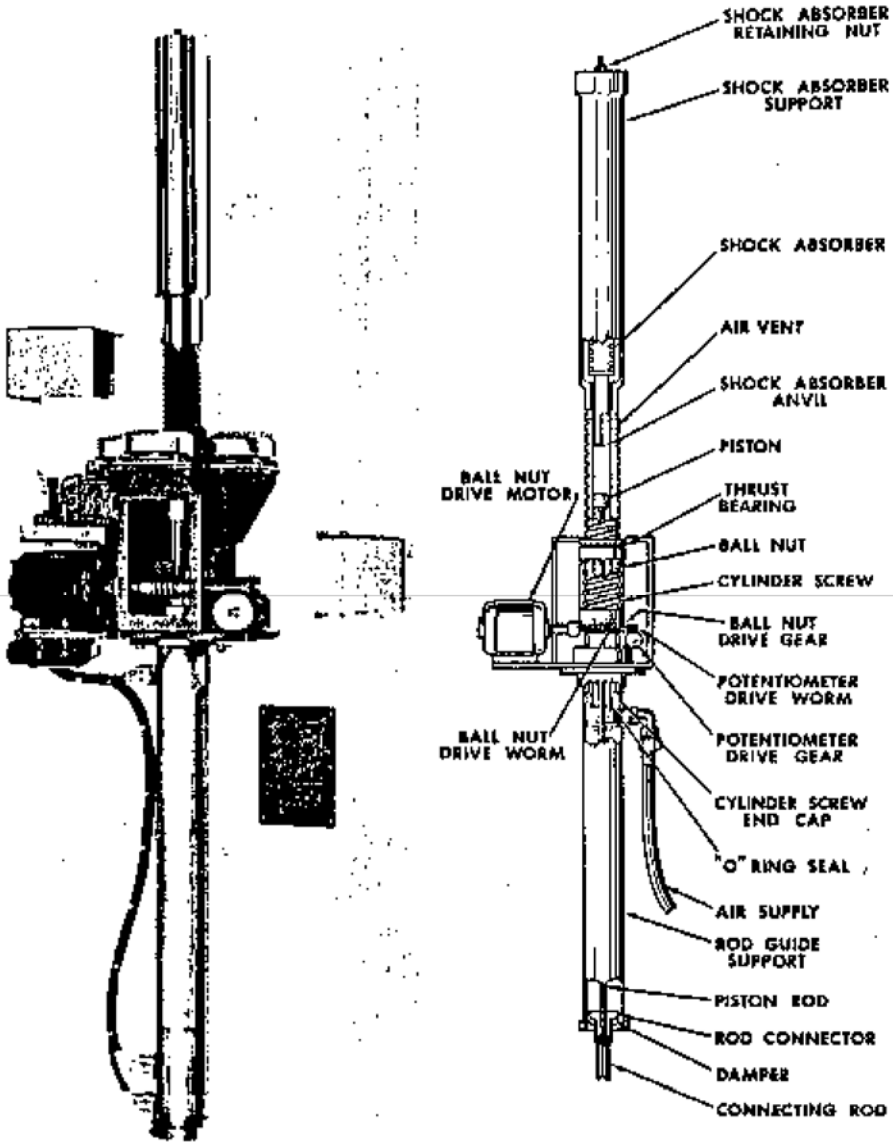


ADJUSTABLE TRANSIENT ROD

Figure 4-32

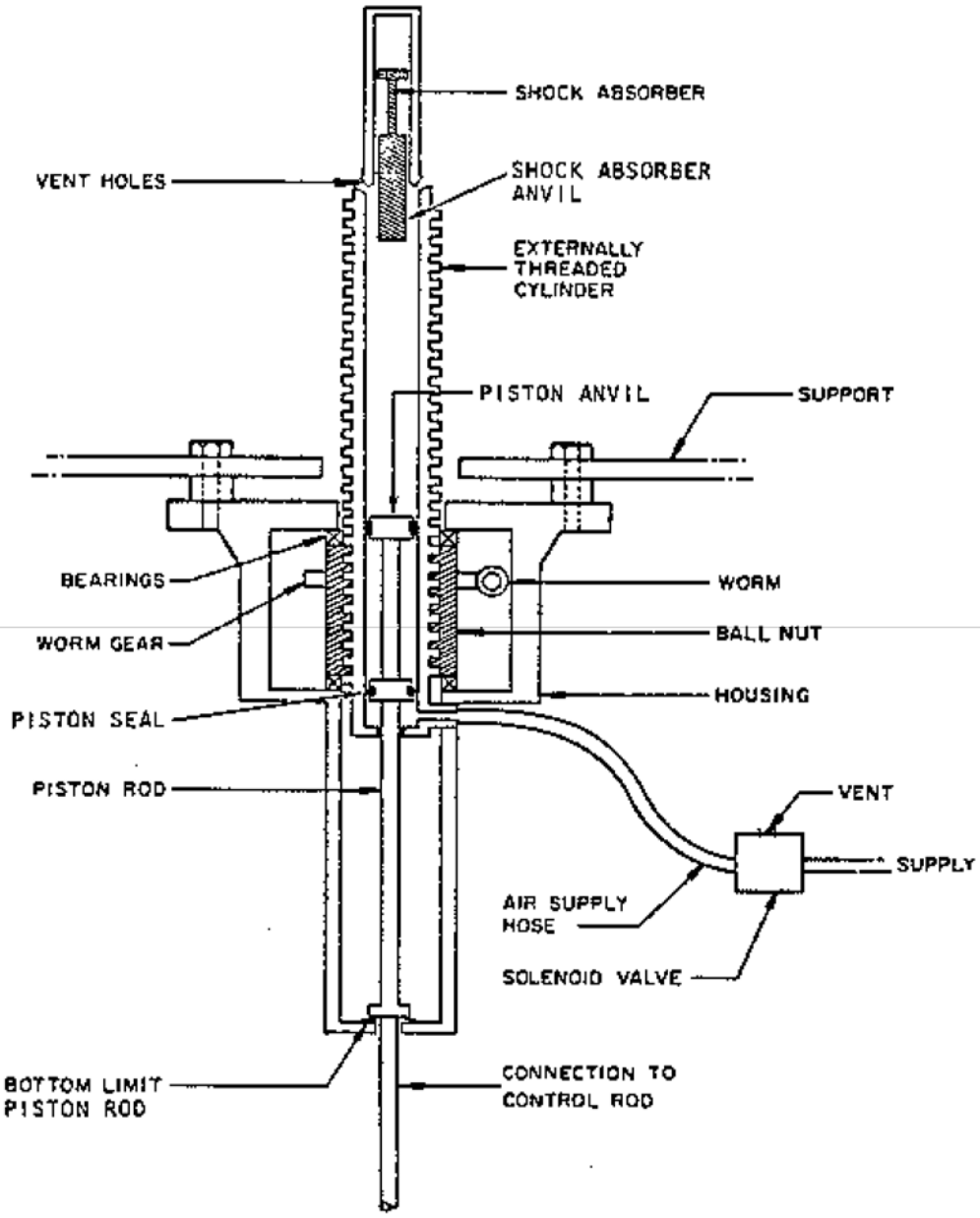


TRANSIENT ROD OPERATIONAL SCHEMATIC

Figure 4-33

The extent of transient rod withdrawal from the core during a pulse is determined by raising or lowering the cylinder, thereby controlling the distance the piston travels.

The cylinder has external threads running most of its length, which engage a series of ball bearings contained in a ball-nut mounted in the drive housing. As the ball-nut is rotated by a worm gear, the cylinder moves up or down depending on the direction of worm gear rotation.

A ten-turn potentiometer driven by the worm shaft provides a signal indicating the position of the cylinder and the distance the transient rod will be ejected from the core. Motor operation for pneumatic cylinder positioning is controlled by a switch on the reactor control console. The magnet power key switch on the control console power supply prevents unauthorized firing of the transient rod drive.

Attached to and extending downward from the transient rod drive housing is the rod guide support, which serves several purposes. The air inlet connection near the bottom of the cylinder projects through a slot in the rod guide and prevents the cylinder from rotating. Attached to the lower end of the piston rod is a flanged connector that is attached to the connecting rod assembly that moves the transient rod. The flanged connector stops the downward movement of the transient rod when the connector strikes the damp pad at the bottom of the rod guide support. A microswitch is mounted on the outside of the guide tube with its actuating lever extending inward through a slot. When the transient rod is fully inserted in the reactor core, the flange connector engages the actuating lever of the microswitch and indicates on the instrument console that the rod is in the core.

In the case of the transient rod a scram signal de-energizes the solenoid valve which supplies the air required to hold the rod in a withdrawn position and the rod drops into the core from the full out position in about 1 second.

4.4.8.4. Evaluation of Control Rod System.

The reactivity worth and speed of travel for the control rods are adequate to allow complete control of the reactor system during operation from a shutdown condition to full power. The scram times for the rods are quite adequate since the TRIGA system does not rely on speed of control as being paramount to the safety of the reactor. The inherent shutdown mechanism of the TRIGA prevents unsafe excursions and the control system is used only for the planned shutdown of the reactor and to control the power level in steady-state operation.

## 4.5 SAFETY SETTINGS IN RELATION TO SAFETY LIMITS

As has been indicated, fuel temperatures are the main safety considerations in the operation of the TRIGA system. The temperature of the fuel may be controlled by setting limits on other operating parameters. The operating parameters of interest for TRIGA are:

a. Maximum licensed steady-state power level

b. Fuel temperature measured by thermocouple

c. Maximum reactivity worth of transient rod

d. Core inlet coolant water temperature

The safety settings as listed in Table 4-12 are such that in all operation, normal and abnormal, the safety limits indicated in the reactor design bases will not be exceeded.

Table 4-12

TRIGA SAFETY SETTINGS

| Parameter Limited | Safety Setting | Function |
|---|---|---|
| Maximum steady-state power level | 1100 kW (t) | Reactor scram |
| Maximum measurement of fuel temperature | 500°C | Reactor scram |

Administrative limitations are imposed for the excess reactivity, transient conditions and coolant water temperature as follows:

a. Maximum core excess reactivity of 4.9% $\delta k/k$ with a shutdown margin of at least 0.2% $\delta k/k$, assuming one rod withdrawn.

b. Maximum transient control rod worth of 2.8% $\delta k/k$ with a limit of 2.2% $\delta k/k$, for any transient insertion.

c. Core inlet water temperature of 48.9°C.

These safety settings are conservative in the sense that if they are adhered to, the consequence of normal or abnormal operation would be fuel and clad temperatures well below the safety limits indicated in the reactor design bases. Because of the conservatism in these safety settings, it is reasonable that at some later date less restrictive safety system settings could be assigned in conjunction with upgrading of the reactor to operate at higher steady-state power levels or in the pulsing mode, while still using the same fuel and core configuration.

## Chapter 4 References


1. Merten, U., et al., "Thermal Migration of Hydrogen in Uranium-Zirconium Alloys," General Dynamics, General Atomic Division Report GA-3618, 1962.

2. Coffer, C. O., et al., "Research in Improved TRIGA Reactor Performance, Final Report," General Dynamics, General Atomic Division Report GA-5786, 1964.

3. Johnson, H. A., et al., "Temperature Variation, Heat Transfer, and Void Volume Development in the Transient Atmosphere Boiling of Water," SAN-1001, University of California, Berkeley, 1961.

4. McAdams, W. H., Heat Transmission, 3rd ed, McGraw-Hill Book Co., New York, 1954.

5. Sparrow, E. M. and R. D. Cess, "The Effect of Subcooled Liquid on Film Boiling," Heat Transfer, 84, 149-156 (1962).

6. Speigler, P., et al., "Onset of Stable Film Boiling and the Foam Limit," Int. J. Heat and Mass Transfer, 6, 987-989 (1963).

7. Zuber, W., "Hydrodynamic Aspects of Boiling Heat Transfer," AEC Report AECV-4439, TIS, ORNL, 1959.

8. Rosnehow, W., and H. Choi, Heat, Mass and Momentum Transfer, Prentice-Hall, 1961, pp. 231-232.

9. Ellion, M. E., "A Study of the Mechanism of Boiling Heat Transfer," Jet Propulsion Laboratory Memo. No. 20-88, 1954.

10. Coffer, C. O., et al., "Characteristics of Large Reactivity Insertions in a High Performance TRIGA U-ZrH Core," General Dynamics, General Atomic Division Report GA-6216, 1965.

11. Fenech, H., and W. Rohsenow, "Thermal Conductance of Metallic Surfaces in Contact," USAEC NYO-2130, 1959.

12. Graff, W. J., "Thermal Conductance Across Metal Joints," Machine Design, Sept. 15, 1960, pp. 166-172.

13. Fenech, H., and J. J. Henry, "An Analysis of a Thermal Contact Resistance," Trans. Am. Nucl. Soc. 5, 476 (1962).

14. Bernath, L., "A Theory of Local Boiling Burnout and Its Application to Existing Data," Heat Transfer - Chemical Engineering Progress Symposium Series, Storrs, Connecticut, v. 56, No. 20, 1960.

15. Spano, A. H., "Quarterly Technical Report SPERT Project, April, May, June, 1964," ISO-17030.

16. Dee, J. B., et al., "Annular Core Pulse Reactor," General Dynamics, General Atomic Division Report GACD 6977 (Supplement 2), 1966.

17. Adler, J., et al., "Users and Programmers Manual for the GGC-3 Multigroup Cross Section Code," General Dynamics, General Atomic Division Report GA-7157, 1967.

18. Lenihan, S. R., "GAZE-2: A One-Dimensional, Multigroup, Neutron Diffusion Theory Code for the IBM-7090," General Dynamics, General Atomic Division Report GA-3152, 1962.

19. Dorsey, J. P., and R. Forehlich, "GAMBLE-5 - A Program for the Solution of the Multigroup Neutron-Diffusion Equations in Two Dimensions, with Arbitrary Group Scattering, for the UNIVAC-1108 Computer," Gulf General Atomic Report GA-8188, 1967.

20. Lathrop, D. K., "DTF-IV, A FORTRAN-IV Program for Solving the Multigroup Transport Equation with Anisotropic Scatterings," USAEC Report LA-3373, Los Alamos Scientific Laboratory, New Mexico, 1965.

21. Adler, F. T., G. W. Hinman, and L. W. Nordheim, "The Quantitative Evaluation to Resonance Integrals," in Proc. 2nd Intern. Conf. Peaceful Uses At. Energy (A/CONF. 15/P/1983), Geneva, International Atomic Energy Agency, 1958.

22. Brown, H. D., Jr., Gulf General Atomic, Inc., "THERMIDOR - A FORTRAN II Code for Calculating the Nelkin Scattering Kernel for Bound Hydrogen (A Modification of Robespierre)," unpublished data.

23. Nelkin, M. S., "Scattering of Slow Neutrons by Water," Phys. Rev. 119, 741-746 (1960).

24. McReynolds, A. W., et al., "Neutron Thermalization by Chemically-Bound Hydrogen and Carbon," in Proc. 2nd Intern. Conf. Peaceful Uses at Energy (A/Conf. 15/F/1540), Geneva, International Atomic Energy Agency, 1958.

25. Whittemore, W. L., "Neutron Interactions in Zirconium Hydride," USAEC Report GA-4490 (Rev.), General Dynamics, General Atomic Division, 1964.

26. Bell, J., "SUMMIT: An IBM-7090 Program for the Computation of Crystalline Scattering Kernels," USAEC Report, General Dynamics, General Atomic Division Report GA-2492, 1962.

27. Beyster, J. R., et al., "Neutron Thermalization in Zirconium Hydride," USAEC Report, General Dynamics, General Atomic Division Report GA-4581, 1963.

28. Woods, A. D. B., et al., "Energy Distribution of Neutrons Scattered from Graphite, Light and Heavy Water, Ice, Zirconium Hydride, Lithium Hydride, Sodium Hydride, and Ammonium Chloride, by the Beryllium Detector Method," In Proc. Symp. Inelastic Scattering of Neutrons in Solids and Liquids, Vienna, Austria, Oct. 11-14, International Atomic Energy Agency, 1960.

29. Jordan, D. P., and G. Leppert, "Pressure Drop and Vapor Volume with Subcooled Nucleate Boiling," Int. J. Heat Mass Trans. 5, 751-761 (1962).

30. McAdams, op. cit., pp. 390-392.

31. Levy, S., "Forced Convection Subcooled Boiling-Prediction of Vapor Volumetric Fraction," Int. J. Heat Mass Trans. 10, 961-965 (1967).

32. McAdams, op. cit., p. 392.

33. Bernath, op. cit., pp. 95-116.

34. Simnad, M. T., "The U-$ZrH_x$ Alloy: Its Properties and Use in TRIGA Fuel," GA Project No. 4314, E-117-833, February 1980, pp. 4-1,7.